

Chandra observations of NGC 253. II: On the origin of diffuse X-ray emission in the halos of starburst galaxies

David K. Strickland,^{1,2} Timothy M. Heckman,² Kimberly A. Weaver,³ Charles G. Hoopes,² and Michael Dahlem⁴

ABSTRACT

We present a detailed case study of the diffuse X-ray and H α emission in the halo of NGC 253, a nearby edge-on starburst galaxy driving a galactic superwind. The arcsecond spatial resolution of the ACIS imaging spectroscopy on the *Chandra* X-ray Observatory allows us to study the spatial and spectral properties of the diffuse X-ray emitting plasma, at a height of between 3 and 9 kpc above the disk in the northern halo of NGC 253, with greatly superior spatial and spectral resolution compared to previous X-ray instruments. We find statistically significant structure within the diffuse emission on angular scales down to $\sim 10''$ (~ 130 pc), and place limits on the luminosity of any X-ray-emitting “clouds” on smaller scales. There is no statistically significant evidence for any spatial variation in the spectral properties of the diffuse emission over scales from several ~ 400 pc to ~ 3 kpc. The spectrum of the diffuse X-ray emission is clearly thermal, although with the higher spectral resolution and sensitivity of *Chandra* it is clear that current simple spectral models do not provide a physically meaningful description of the spectrum. In particular, the fitted metal abundances are unphysically low. There is no convincing evidence for diffuse X-ray emission at energies above 2 keV in the halo.

We show that the X-shaped soft X-ray morphology of the superwind previously revealed by *ROSAT* is matched by very similar X-shaped H α emission, extending at least 8 kpc above the plane of the galaxy. In the northern halo the X-ray emission appears to lie slightly interior to the boundary marked by the H α emission. The total 0.3 – 2.0 keV energy band X-ray luminosity of the northern halo $L_X \sim 5 \times 10^{38}$ erg s $^{-1}$, is very similar to the halo H α luminosity of $L_{H\alpha} \sim 4 \times 10^{38}$ erg s $^{-1}$, both of which are a small fraction of the estimated wind energy injection rate of $\sim 10^{42}$ erg s $^{-1}$ from supernovae in the starburst. We show that there are a variety of models that can simultaneously explain spatially-correlated X-ray and H α emission in the halos of starburst galaxies, although the physical origin of the various emission components can be very different in different models. These findings indicate that the physical origin of the X-ray-emitting million-degree plasma in superwinds is closely linked to the presence of much cooler and denser $T \sim 10^4$ gas, not only within the central kpc regions of starbursts, but also on ~ 10 kpc-scales within the halos of these galaxies.

Subject headings: ISM: jets and outflows — ISM: bubbles — galaxies: halos — galaxies: individual (NGC 253) — galaxies: starburst — X-rays: galaxies

¹ *Chandra* Fellow.

²Department of Physics and Astronomy, The Johns Hopkins University, 3400 North Charles Street, Baltimore, MD 21218

³NASA/Goddard Space Flight Center, Code 662, Greenbelt, Maryland 20771

⁴European Southern Observatory, Casilla 19001, Santi-

1. Introduction

NGC 253 is an archetypal starburst galaxy at a distance of only $D = 2.6$ Mpc (Puche & Carignan 1988), and is the closest edge-on IR luminous starburst galaxy ($L_{\text{FIR}} = 1.7 \times 10^{10} L_{\odot}$, Radovich,

ago 19, Chile

Kahanpää & Lemke (2001)). As such it represents the best local laboratory to study the effects of stellar feedback from strong star formation on the gaseous interstellar medium (ISM), processes which are intimately connected to galaxy formation and galaxy evolution.

Potentially the most significant form of stellar feedback is the driving of high-velocity, galactic-scale, multi-phase outflows — “superwinds” (Heckman, Armus & Miley (1990); Heckman, Lehnert & Armus (1993); Bland-Hawthorn (1995)). These supernova-driven outflows are ubiquitous in all local starburst galaxies (Lehnert & Heckman 1996), and there is mounting evidence that they are extremely common in high red-shift galaxies (Pettini et al. 2001).

Among the many implications of superwinds, their possible role in enriching and heating the intergalactic medium (IGM) is currently attracting much attention (e.g. Nath & Trentham (1997); Ferrara, Pettini & Shchekinov (2000); Lloyd-Davies, Ponman & Cannon (2000)). For an up-to-date review see Heckman (2001)).

X-ray observations of superwinds can in principle tell us much about the energetics and composition of these outflows, and hence the transport of energy and metal-enriched gas into the IGM. Superwinds are driven by the thermal pressure of hot (up to $T \sim 10^8\text{K}$) thermalized SN-ejecta, gas which is expected to be highly metal-enriched. Adiabatic expansion cools the gas, converting the thermal energy into bulk motion at velocities up to $v \sim 3000\text{ km/s}$. Gas over-run by the expanding wind, either within the disk or the halo, may be shock-heated to million degree temperatures and itself become a source of thermal X-ray emission (Chevalier & Clegg 1985). Other processes, such as thermal conduction or turbulent mixing between cool dense gas and surrounding hot regions, can also lead to X-ray-emitting interface regions (Weaver et al. 1977).

The hydrodynamical complexity of these outflows (see e.g. (Suchkov et al. 1994); Strickland & Stevens (2000)), and in particular the range of possible physical mechanisms generating X-ray emission in starburst galaxies, has complicated the interpretation of existing X-ray observations of starburst galaxies with superwinds with the low spatial-resolution instruments that were available before the launch of the *Chandra* X-ray Obser-

vatory in 1999 (see the discussions in Dahlem, Weaver & Heckman (1998); Strickland & Stevens (2000); Weaver, Heckman & Dahlem (2000); Strickland et al. (2000)).

In this paper we present a detailed case study of the diffuse X-ray emission from the superwind that extends $\sim 10\text{ kpc}$ into the northern halo of NGC 253 with *Chandra*. Our aim is to use this data, along with deep ground-based optical $\text{H}\alpha$ imaging, to investigate the physical origin of the extended soft thermal X-ray emission seen in a *typical* starburst-driven superwind.

The fundamental advantage *Chandra* offers over any other previous or currently-existing instrument is $\sim 1''$ -spatial resolution ($1'' \approx 13\text{ pc}$ at the distance of NGC 253), ~ 10 times better spatial resolution than *XMM-Newton*. This allows us to robustly remove emission from unrelated point sources and resolve out any spatial variations in the spectral properties of the diffuse emission. With *Chandra* we can obtain *spatially-resolved spectroscopy of diffuse emission alone*. In contrast, *ASCA*, *BeppoSAX* or combined *ROSAT* PSPC and *ASCA* spectroscopy invariably covered the entire galaxy, including all point source and possible AGN emission (e.g. Persic et al. (1998); DWH98). In addition, the spectral resolution of *Chandra* is comparable to spectral studies with *ASCA* (Ptak et al. 1997) and significantly better than that of the *ROSAT* PSPC-based studies of superwinds (Read (1994); Read, Ponman & Strickland (1997); Pietsch et al. (2000)).

This work follows on from our *Chandra* study of the diffuse X-ray emission in the central kiloparsec of NGC 253, which explored the brighter inner-most part of the superwind (Strickland et al. 2000).

2. Observations and data analysis

2.1. X-ray observations

Guest observer observations of NGC 253, using the AXAF CCD Imaging Spectrometer (ACIS⁵) on board the *Chandra* X-ray Observatory, were obtained on 1999 December 16 (*Chandra* ObsID

⁵For more information on the capabilities of *Chandra* and ACIS see the *Chandra* Observatory Guide <http://asc.harvard.edu/udocs/docs/docs.html>, section “Observatory Guide”, “ACIS”

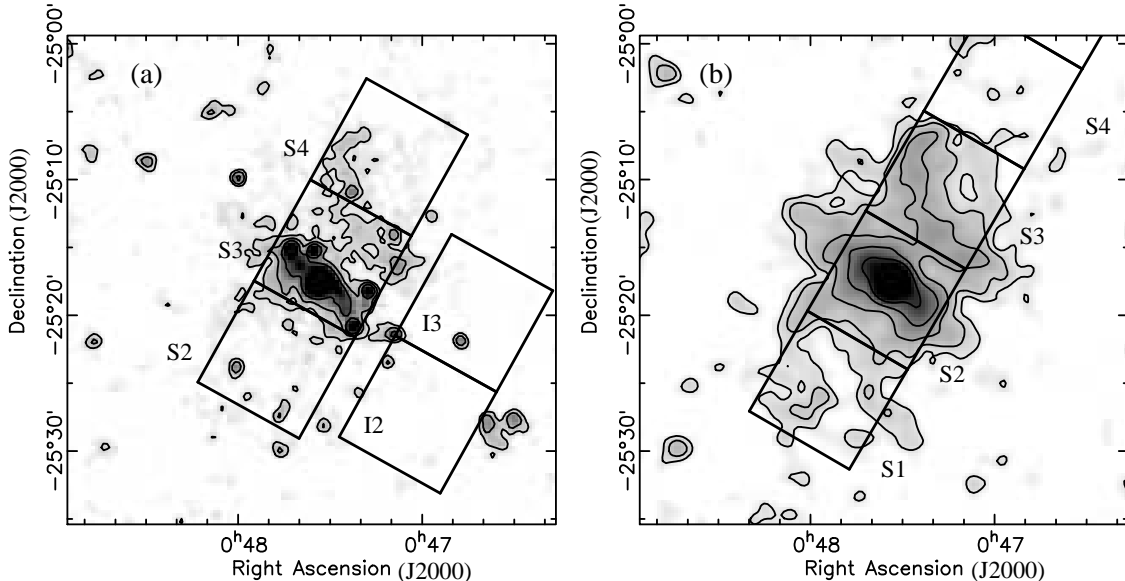


Fig. 1.— *ROSAT* PSPC images of NGC 253, showing the position of the ACIS chips in the two *Chandra* observations with respect to the large scale diffuse X-ray emission from the superwind. (a) ACIS chip orientation in the ~ 13 ks observation (*Chandra* ObsID 969), overlaid on the 0.1 – 2.0 keV *ROSAT* PSPC image. The PSPC image has been smoothed with a FWHM = 35'' Gaussian mask, and is shown on a logarithmic intensity scale between 10^{-4} and 10^{-2} counts s^{-1} arcmin $^{-2}$. Contours are shown at a surface brightness levels of 1.6, 3.2 and 6.4×10^{-3} counts s^{-1} arcmin $^{-2}$. (b) ACIS chip orientation in the ~ 43 ks observation (*Chandra* ObsID 790), overlaid on the 0.1 – 2.0 keV *ROSAT* PSPC image from which all the *ROSAT*-detected point sources have been removed (except in the nucleus of the galaxy) and the resulting gaps in the data interpolated over. This image provides a better representation of the large-scale diffuse emission. The image has been smoothed with a FWHM = 70'' Gaussian mask, and is shown using the same logarithmic intensity scale as in panel (a). Contours are shown at surface brightness levels of 0.4, 0.8, 1.6 and 3.2×10^{-3} counts s^{-1} arcmin $^{-2}$.

969) and December 27 (ObsID 790), resulting in a total exposure time on the S3 chip (prior to the removal of background flares described in § 2.1.2) of 13987 and 43522 seconds respectively. The back-illuminated S3 CCD was at the focal point of the telescope, as it is more sensitive to the low energy X-ray photons from the superwind than the front illuminated ACIS chips. The observations were positioned so as to place the disk of the galaxy, and the starburst nucleus, within the S3 chip in the shorter exposure, and the northern lobe of the superwind in the S3 chip in the longer exposure. Figure 1 shows the orientation and position of the ACIS chips on the sky, overlaid on a 0.1 – 2.0 keV

energy band image of the *ROSAT* PSPC⁶ data.

Compared to the *ROSAT* PSPC (the only previous instrument able to attempt spatially-resolved spectroscopy on diffuse emission in the halos of superwinds) observations of NGC 253, our ACIS observations have count rates ~ 3 times higher and twice the total exposure length, in addition to covering a much wider energy range at ~ 30 times the spatial resolution.

The ACIS instrument is an imaging CCD spectrometer, comprising two back-illuminated CCD chips (chips S1 & S3, nominal in-flight spectral resolution of ~ 0.12 keV at a photon energy of 1.5

⁶The *ROSAT* PSPC data was obtained from the HEASARC archive, and reduced using the Extended Source Analysis Software created by Steve Snowden.

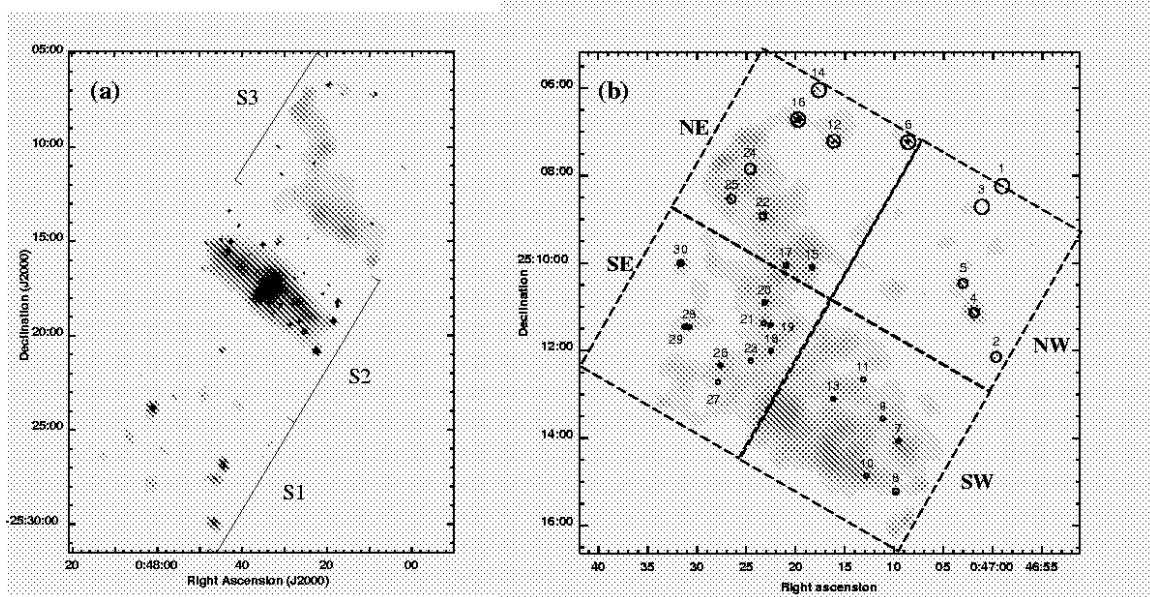


Fig. 2.— (a) An adaptively smoothed 0.3 – 8.0 keV image of ACIS chips S1, S2 & S3 from observation ObsID 790. (b) Adaptively-smoothed 0.3 – 8.0 keV image of the northern halo region on the S3 chip, showing the regions chosen for diffuse emission analysis (Table 1) along with all point sources with $S/N \geq 2$ (Table 7). Both images are shown on a logarithmic intensity scale, and have been smoothed so that features are locally significant at $\geq 5\sigma$ in panel (a) and significant at $\geq 3\sigma$ in panel (b).

keV, at the CCD temperature of -110°C at which the observations of NGC 253 were taken), and eight front-illuminated CCD chips (these chips were damaged by cosmic rays. Their degraded in-flight spectral resolution ranges from 0.09 keV to 0.18 keV at a photon energy of 1.5 keV, and depends on the location within the chip). Each chip is 1024 pixels square, with a plate scale of $0''.492$ per pixel. The spatial resolution of the instrument is $\approx 0''.8$ (FWHM) on the optical axis with the ACIS-S array in the focal plane, and degrades to $\sim 6''$ at an off axis angle of $6'$.

The properties of the diffuse emission in the northern halo of NGC 253 reported in this paper are based exclusively on S3 chip data from the longer observation. The halo region does fall within the S4 chip in the shorter *Chandra* observation, but inspection of the data reveals that it adds nothing to what can be obtained from the targeted S3 observation of the halo. The combination of a shorter exposure time, a larger off-axis angle leading to a lower spatial resolution, and a CCD read-out problem with the S4 chip that requires additional event filtering, all conspire to make the S4

chip data on the halo superfluous compared to the longer observation.

The southern halo of NGC 253 is partially covered by the back-illuminated S1 chip in our longer observation. As the center of the S1 chip is $\sim 14'$ off-axis, the point spread function (PSF) of the telescope is large⁷ and comparable in size to the PSF of *XMM-Newton* or the *ROSAT* PSPC, making it difficult to identify and remove point sources from the data. The diffuse emission in this region is also fainter than in the northern halo (as can be seen in Figs. 1 & 2), and analysis of the *Chandra* data reveals no significant structure to the diffuse emission. For these reasons we have chosen to concentrate upon the higher quality data from the northern halo.

The data was reduced and analyzed using CIAO (version 2.1), HEASOFT (version 5.0.2) and XSPEC (version 11.0.1a.j). The latest *Chandra* calibration files available for this observation were used

⁷The 50%-energy enclosed radius of the *Chandra* PSF varies between $0''.4$ and $3''.5$ over the S3 chip, and grows to between $7''$ to $21''$ within the S1 chip.

TABLE 1
SPATIAL REGIONS USED WITHIN NGC 253 AND ITS HALO

Region	α (J2000) (h m s)	δ (J2000) ($^{\circ}$ ' ")	Roll (deg)	Angular size ($'' \times ''$)	Physical size (kpc \times kpc)	Area (arcmin 2)		Distance from nucleus ($''$) (kpc)	
(1)	(2)	(3)	(4)	(5)	(6)	(7)	(8)	(9)	(10)
Halo	00 47 16.43	-25 10 49.49	330	503.8 2	6.35 \times 6.35	70.506	69.713	449.2	5.66
NE halo	00 47 19.92	-25 07 57.90	330	251.9 2	3.18 \times 3.18	17.627	17.187	587.4	7.40
NW halo	00 47 03.74	-25 10 03.39	330	251.9 2	3.18 \times 3.18	17.627	17.391	589.6	7.43
SE halo	00 47 29.17	-25 11 35.29	330	251.9 2	3.18 \times 3.18	17.627	17.545	346.1	4.36
SW halo	00 47 12.99	-25 13 43.00	330	251.9 2	3.18 \times 3.18	17.627	17.579	347.6	4.38
Disk ^a	00 47 33.12	-25 17 17.57	330	503.8 \times 251.9	6.35 \times 3.18	35.252	31.827	0.0	0.0

NOTE.—Columns (2) & (3): Coordinates of the center of the region. (4): *Chandra* observation roll angle. (5 & 6): Projected size of the region in arcsec (5) and kpc (6) within the plane of the sky, assuming a distance of 2.6 Mpc to NGC 253. (7): Total geometrical area of the region. (8): Geometrical area remaining after point source removal. (9 & 10): Projected distance from nucleus (the brightest radio source in Ulvestad & Antonucci (1997)) to the center of the region in arcsec (9) and kpc (10).

^aIn addition to excluding all point sources, we used a rectangular region of total length 180 $''$ along the minor axis of the galaxy by 60 $''$ wide, centered on the brightest nuclear radio source, to exclude the bright diffuse emission from nuclear starburst region and the nuclear outflow cones.

(CALDB version 2.3). The known problems with these calibration files are discussed in § 2.1.5. Our reduction and processing followed the guide lines released by the CXC and the ACIS instrument team⁸.

2.1.1. Background images and spectra

We have used the background event data sets provided by the CXC to obtain background images and spectra for the S3 chip. We can not obtain a local estimate of the background from our data alone as the diffuse emission in the halo of NGC 253 fills the entire S3 chip. The background data set used provided a total exposure in the S3 chip of 114886 s, so the statistical uncertainties in the background counts are significantly reduced compared to using a local background estimate.

The disadvantage of using data taken at different times and along different sight lines is that one must worry about systematic differences between the background in our observation and that in the datasets used to create the blank-sky background data. We believe this systematic effect is only significant at photon energies $E > 2$ keV, for the reasons we discuss later.

⁸The CIAO (v2.1) Science Threads can be found at http://asc.harvard.edu/ciao/documents_threads.html, the ACIS instrument team’s recipes at <http://www.astro.psu.edu/xray/acis/recipes/>.

2.1.2. Time filtering and flare removal

We filtered out periods of enhanced total count rate (“flares”) due to low energy protons interacting with the detector. We identified and excluded periods of higher (or lower) than average count rate by creating a light curve of all events falling with the S3 chip and using two iterations of a 5σ -clipping technique to identify outliers and obtain an accurate measurement of the mean “quiescent” count rate. Following the advice of Maxim Markevitch (Markevitch 2000, private communication) we binned the light curve into 258.28 second-long bins, which corresponds to exactly 80 CCD exposures. This time filtering resulted in a total useful exposure of 39588.3 s, a loss of 9.0% of the data. Inspection of the resulting filtered light curve showed all obvious broad-energy-band flaring had been removed.

2.1.3. Point source identification

The standard source searching methods provided as part of CIAO gave unsatisfactory results when used on the mix of point sources and diffuse emission we find in these observations. Large numbers of possibly spurious sources were identified at low, but still sensible, signal-to-noise ratios by both the sliding box-based CELLDETECT and the wavelet-based WAVDETECT source searching programs, (different sources being found depending

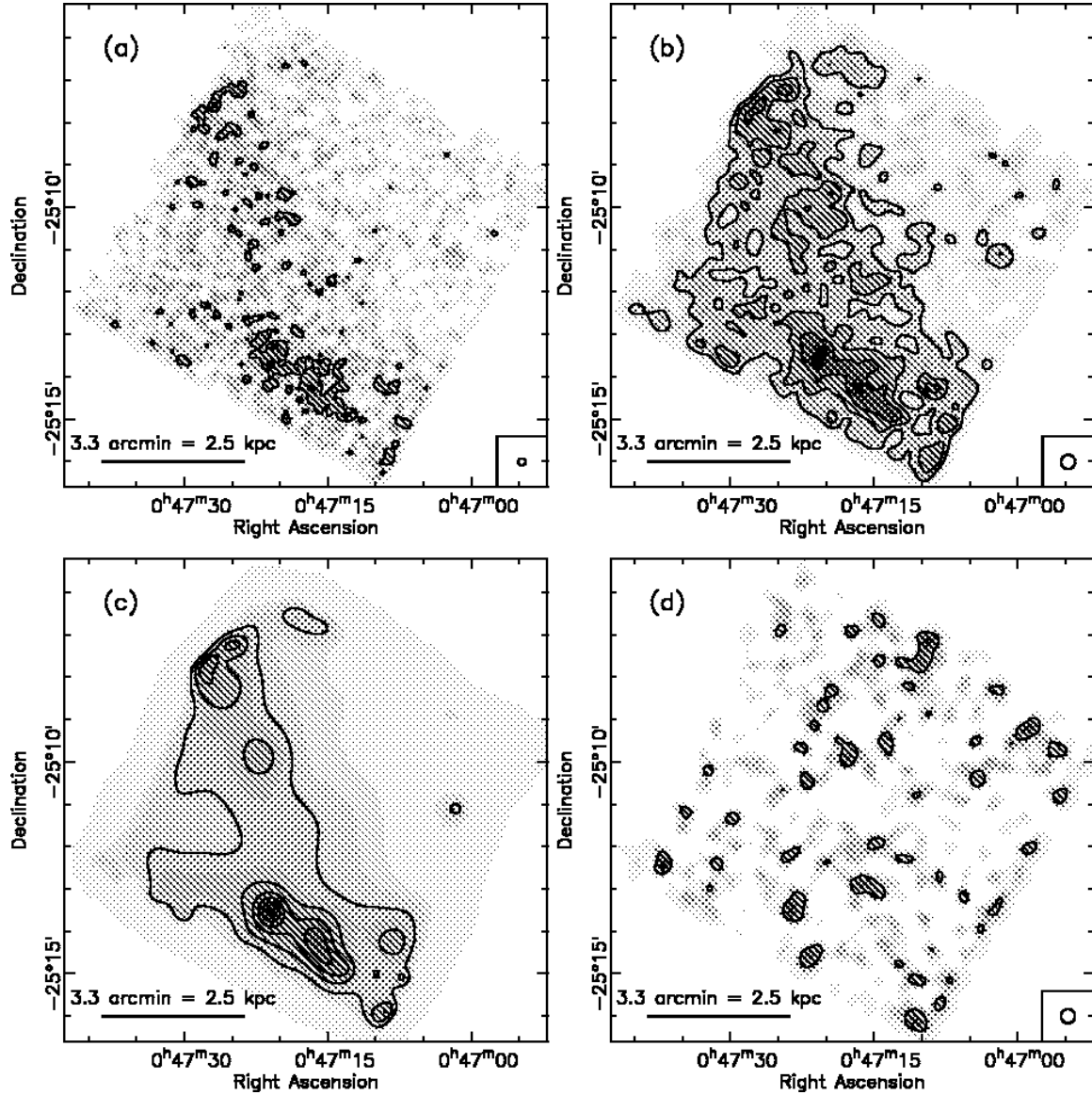


Fig. 3.— *Chandra* ACIS-S3 images of the diffuse X-ray emission in the northern halo. Point sources and background emission have been subtracted from the data. Panels (a) to (c) show soft X-ray emission in the 0.3 – 2.0 keV energy band, while (d) is a 2.0 – 8.0 keV energy band hard X-ray image. All images use a linear intensity scale from zero surface brightness to the maximum surface brightness found in that image. (a) The soft diffuse emission smoothed with a $FWHM = 10''$ Gaussian mask (the diameter of open circle at the bottom right of the image shows the FWHM of the mask). Contours are shown at signal-to-noise values of 2 and 3 above the background in a $10''$ -diameter aperture (see Table 9 for the relationship between surface brightness and signal-to-noise ratio). (b) As (a), except smoothed with a $FWHM = 20''$ Gaussian mask to emphasize the larger-scale diffuse emission. Contours are shown at signal-to-noise ratios of 2, 3, 4 & 5 within a $20''$ -diameter aperture. (c) An adaptively-smoothed image of the diffuse soft X-ray emission. Structures visible in this image are significant at the 3σ level above the local diffuse emission and background. Contours are shown at $0.9, 1.35, 1.80, 2.25$ & 2.70×10^{-6} counts s^{-1} arcsec $^{-2}$. (d) The hard X-ray emission remaining after point source and background subtraction, smoothed with a $FWHM = 20''$ Gaussian. Contours are shown at signal-to-noise ratios of 1 & 2 within a $20''$ -diameter aperture. There does not appear to be any significant detection of diffuse hard X-ray emission from the halo.

on which method was used). These extra sources are found preferentially in regions where the diffuse X-ray emission is brightest, suggesting that

these excess sources were mis-identification of diffuse emission as point sources. To obtain robust point source identifications we used the scheme de-

scribed in Appendix A.

2.1.4. Spectral fitting

ACIS spectra were extracted using Pulse Invariant (PI) data values, in order to account for the spatial variations in gain between different chip nodes. In order to use χ^2 as the fit statistic the spectra were binned to give a minimum of 10 counts per bin after background subtraction.

Spectral responses were created using the latest calibration files available at the time of writing for observations taken with the CCD temperature of -110°C (CALDB version 2.3), following the example procedures provided by the CXC.

2.1.5. Calibration uncertainties

The calibration of the ACIS instrument used at the time of writing was the best available, but is known to be deficient in a number of ways.

1. **Low energy effective area:** The low energy effective area of the S3 chip is uncertain. This will impact fitting absorbing hydrogen columns, which in turn affects the inferred absorption-corrected fluxes and emission integrals.
2. **Energy scale below 1 keV:** The energy scale of the ACIS S3 chip is believed to be ~ 20 eV too low at energies below 1 keV. We have taken this into account by fitting for the energy offset using the GAIN command in XSPEC, although we stress this is method of correction can only be considered an approximation.
3. **Energy resolution:** The width and shape of line features in the current spectral response differ from those observed. In particular the spectral responses appear to systematically underestimate the width of spectral features by up to 40%.

These will affect spectral fitting of the data, although not to a degree that precludes any analysis of the data. We will discuss the effect these calibration problems have on our spectral analysis in § 4. We wish to emphasize that these calibration uncertainties have negligible effect on the image-based analysis of the data.

2.2. Optical $H\alpha$ and R-band imaging

Two sets of ground-based optical imaging of NGC 253 were used to investigate whether NGC 253 has a large scale $H\alpha$ emitting halo, and to investigate the absolute astrometric accuracy of the *Chandra* data.

The first data set is a mosaic of previously unpublished R-band and $H\alpha$ images taken by us with the 4m telescope at CTIO, which only partially cover the region of these *Chandra* observations.

The second set of images were taken with the 0.6m Curtis/Schmidt telescope at CTIO, taken as part of a survey of the diffuse ionized gas in Sculptor group galaxies (Hoopes, Walterbos & Greenawalt 1996). These images are less sensitive than the 4m imaging, but cover a larger field of view and form the basis of our X-ray/ $H\alpha$ comparison study described in § 6.

The narrow-band $H\alpha$ filter used has a peak transmission at 6570 \AA and FWHM of 68 \AA . The telescope optics cause the filter passband to be blue-shifted by $\sim 10 \text{ \AA}$. Combined with a 5 \AA red-shift due to the systematic velocity of NGC 253, this places the $H\alpha$ line and the weak [NII] 6548 \AA line near the peak of the filter transmission, and the stronger [NII] 6584 \AA line at $\sim 50\%$ of the peak filter transmission. Continuum subtraction was performed using images from a 77 \AA wide continuum filter centered at 6649 \AA .

We flux-calibrated the resulting continuum-subtracted line image using the spectrophotometric measurement of the $H\alpha$ and [NII] fluxes in a $8''.1$ -diameter region centered on the nucleus, from (Keel 1984). In creating a fluxed $H\alpha$ surface brightness image we have assumed that the [NII]/ $H\alpha$ flux ratio is always 0.63, the value Keel (1984) found within the nuclear region. Any increase, or decrease, in the [NII]/ $H\alpha$ flux ratio will introduce an error into the $H\alpha$ fluxes we quote in this paper.

Based on observations of edge-on spiral galaxies it is known that the [NII]/ $H\alpha$ flux ratio typically increases with height above the plane. For example, Rand (1998) finds [NII]/ $H\alpha \sim 1 - 1.5$ at $z \sim 2$ kpc above the plane of NGC 891, and Tüllmann et al. (2000) find values of [NII]/ $H\alpha \sim 1.0 \pm 0.1$ at $z \sim 8$ kpc above the plane of the (possibly starbursting) spiral galaxy NGC 5775. Unfortunately, there are no published spectroscopic mea-

measurements of the $[\text{NII}]/\text{H}\alpha$ flux ratio high in the halo of NGC 253. Bland-Hawthorn, Freeman & Quinn (1997) measure a $[\text{NII}]/\text{H}\alpha$ flux ratio of ~ 1 at large radii in the plane of NGC 253's disk, beyond the optical edge of the disk, although this ionized gas may be unrelated to that in the halo of NGC 253. To give the reader a feeling of the uncertainty this introduces into the $\text{H}\alpha$ fluxes and luminosities we quote later in this paper, if $[\text{NII}]/\text{H}\alpha = 1.5$ at any point, our estimate, using the fixed ratio $[\text{NII}]/\text{H}\alpha = 0.63$, would over-estimate the true $\text{H}\alpha$ flux by 40%.

For further details of the narrow-band observations and the associated data reduction we refer the reader to Hoopes, Walterbos & Greenawald (1996).

2.2.1. X-ray/optical counterparts and astrometric accuracy

We looked for optical counterparts to the *Chandra* X-ray sources in both sets of R-band CCD images. We used the online catalog of the APM survey (Maddox et al. 1990) to obtain coordinates for stars visible in the both sets of CCD images, and hence obtain astrometric solutions for the CCD images. The rms uncertainty in the absolute positions in the optical CCD images is $0''.15$ (4m images) and $0''.20$ (0.6m images).

Comparison between the X-ray positions and the positions of the 12 optical counterparts found in the S3 chip field of view, taken from the APM catalog, indicates that the absolute coordinates in the default *Chandra* astrometry are accurate to $\sim 0''.7$. As greater accuracy is unnecessary for our purposes, we have not further corrected the *Chandra* astrometric solution. All X-ray source positions quoted in this paper are based on the default astrometry.

3. Spatial morphology of the diffuse X-ray emission in the northern halo

The soft X-ray ridge or arc seen in earlier *ROSAT* observations of NGC 253 is clearly visible in the *Chandra* data from energies below ~ 2 keV (see Figs. 2b & 3). Although there appears to be an excess of point-like sources detected within the ridge, this is a coincidence. The number of point sources detected within the halo is consistent with the number expected based on deeper *Chan-*

dra surveys of the X-ray background (Giacconi et al. 2001). The point sources are discussed in more detail in § 5.

Based on the *Chandra* and *ROSAT* data it is tempting to interpret the eastern edge of the ridge as the limb-brightened edge of the wind – this possibility is discussed in § 7.1. The spatial resolution of the *ROSAT* PSPC data is not high enough to conclusively prove that the ridge marks a sharp boundary to the region of X-ray emitting plasma in the east. Unfortunately the limited angular coverage of the existing *Chandra* data does not extend far enough to the east. *XMM-Newton* observations will better constrain the larger scale morphology of the diffuse emission, although the only published description of the *XMM-Newton* Performance Verification (PV) phase observations (Pietsch et al. 2001) of NGC 253 only discusses the disk of the galaxy.

The relationship between the diffuse X-ray emission and optical $\text{H}\alpha$ emission is explored in more detail in § 6.

Although the ridge feature dominates the total X-ray flux from the northern halo, there is diffuse emission away the ridge. The mean X-ray surface brightness in the north west quadrant of the halo region is only a factor 2 – 3 lower than the mean surface brightness within the ridge. If we interpret the ridge in terms of limb-brightening, the emission that apparently lies within the interior of the wind may be from the front and rear walls of the wind.

Previous instruments sensitive to X-rays at energies higher than 2 keV (*ASCA*, *BeppoSAX*) did not have sufficient spatial resolution to determine if there was any diffuse X-ray emission at these energies (despite some claims to the contrary, e.g. Persic et al. (1998)). Within our significantly more sensitive observation of the halo there is only a marginal 3.3σ detection of diffuse X-ray flux over the entire halo region at energies between 2 – 8 keV. The ACIS images clearly show (Fig. 3d) that no spatial structure is visible at photon energies greater than 2 keV, once point sources have been removed from the data. It is likely that the hard X-ray emission is not related to NGC 253, but is an artefact of the background subtraction (see § 4).

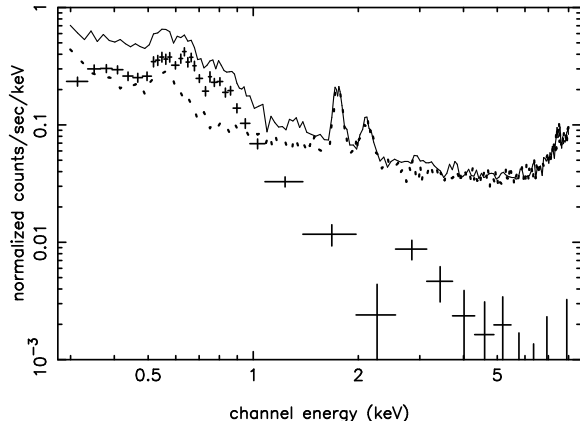


Fig. 4.— The diffuse emission (*i.e.* point source-subtracted) ACIS-S spectrum of the northern halo region (solid line), predicted background (dotted line) and background-subtracted diffuse spectrum (crosses) for the northern halo region. Strong instrumental features (e.g at $E = 1.8$ and 2.0 keV) are well subtracted using the background dataset spectrum. The residual emission in the background-subtracted diffuse spectrum at $E \sim 3$ keV is unlikely to be a real feature of the X-ray emission from the superwind.

4. Spectral properties of the diffuse X-ray emission

We expect thermal X-ray emission from superwinds, from both physical (see § 1) and empirical reasons. Earlier X-ray spectroscopy of superwinds, including NGC 253, although best fit by simple thermal models, gave perplexing results. These spectral fits appeared to imply unphysically low metal abundances (Ptak et al. (1997); Tsuru et al. (1997)), with iron and α -element abundances $\sim 1/20$ and $\sim 1/3$ of the Solar value. Fitting simple models to X-ray spectra where there are a range of gas temperatures or different amounts of absorption can lead to systematically underestimated metal abundances (see DWH98; Strickland & Stevens (1998); Weaver, Heckman & Dahlem (2000)), which may explain the anomalously low abundances of the earlier X-ray studies. Accurate abundance determinations are vital for obtaining accurate estimates of important plasma properties, as the emission integral ($EI = \int n_e n_H dV$) trades off directly with the abundance in the spectral fitting process.

We have therefore expended significant effort in constraining the degree of spatial variation in the spectral properties of the diffuse emission. If it is possible to spatially resolve, and hence separate, these spectrally distinct regions to obtain less complex spectra then more robust estimates of the physical properties of the X-ray emitting plasma may be obtainable.

Other plausible explanations for low gas phase abundances are that emission comes from relatively unenriched halo gas that has never been in the disk of the galaxy, or that sputtering is ineffective at removing the refractory elements from dust grains. Both of these hypotheses can be tested by comparing the derived abundances of the gas in the halo with that from the disk, and comparing abundances of weakly-or-non-depleted elements, e.g. oxygen, to the abundances of refractory elements such as iron.

We discuss the gross spectral characteristics of the halo diffuse emission, in comparison the diffuse thermal emission from the nuclear outflow cone and the diffuse emission within the disk of NGC 253, in § 4.1. In § 4.2 we investigate whether there is any spatial variation in the spectral properties of the emission within the halo. Finding no significant variation on any spatial scale, we investigated the spectral properties of the diffuse emission summed over the entire chip by fitting various spectral models to the data (§ 4.3). As it is easier to predict a-priori the metal abundance of the X-ray-emitting plasma in the disk of the galaxy we compare the derived spectral properties of the halo to those of the diffuse X-ray emission in the disk of the galaxy. Finally, we use the results of this model fitting to obtain crude estimates of the physical properties of the X-ray emitting plasma (§ 4.4).

4.1. Spectral characteristics of the halo

The diffuse X-ray spectrum (*i.e.* after emission due to point sources and the background has been subtracted) of the entire northern halo region is dominated by emission below photon energies of 1 keV (see Fig. 4). This is consistent with the earlier ROSAT PSPC results, which characterized the emission from the halo as soft thermal emission with $kT \sim 0.2$ keV. Features attributable to spectrally-unresolved line emission from highly ionized oxygen, magnesium and possibly iron are

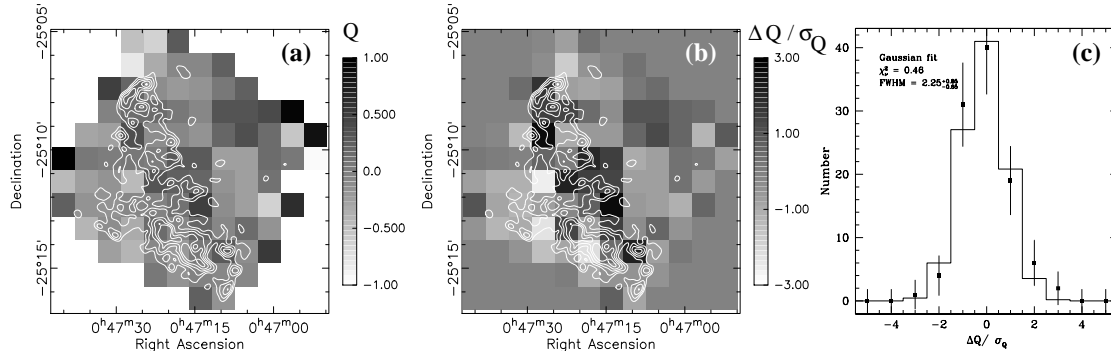


Fig. 5.— Spatial variation in spectral properties of the diffuse emission in the northern halo: (a) The halo diffuse emission hardness ratio $Q = (H - S)/(H + S)$ as a function of position, where the hard energy band $H = 0.6 - 1.0$ keV and the soft energy band $S = 0.3 - 0.6$ keV. The contours show the $20''$ -FWHM smoothed $0.3 - 2.0$ keV image. The mean hardness over the entire chip is $Q_{\text{mean}} = -0.035 \pm 0.018$. (b) The hardness ratio deviation significance $\Delta Q / \sigma_Q$ map. (c) The number distribution of hardness ratio deviation significances $\Delta Q / \sigma_Q$ for the diffuse halo emission, fit by a Gaussian model.

visible in the spectrum, although much weaker than would be expected for a Solar-metallicity hot plasma. This spectrum looks very similar to that of the halo region of NGC 4631 (see Fig. 3 in Wang et al. (2001)), another star-forming galaxy that most probably also hosts a superwind outflow. The ACIS spectrum of NGC 253’s southern nuclear outflow cone (Strickland et al. 2000) is spectrally harder (and therefore presumably hotter and/or more absorbed) than the diffuse emission in the halo.

Interestingly, there appears to be very little diffuse emission at energies above 2 keV. Prior to *Chandra* it was impossible to obtain information on the diffuse emission from superwinds due to contamination from point source emission using older, lower spatial resolution, instruments such as *ASCA*.

The diffuse spectrum shown in Fig 4 shows a peculiar bump in the spectrum at $E \sim 3$ keV, which can not easily be attributed to either emission from the superwind itself or explained as an instrumental feature. Instrument-related features due to silicon in the non-background subtracted spectrum ($E \sim 2$ keV) subtracted out almost perfectly, suggesting the 3 keV bump is not a feature present in all ACIS data. Unresolved line emission from hydrogen-or-helium-like argon would appear at approximately 3 keV, but to explain this feature as argon emission from the superwind would require argon abundances $\gtrsim 20$ times the Solar value, which is highly unlikely given that we do not see such strong spectral features from the other α -

elements.

Emission associated with periods of enhanced background in the detector (“flares”) can lead to apparent excesses at energies between 2 – 4 keV (Markevitch 2000, private communication). We experimented with more stringent filtering of the data to remove flares, but both the 2 – 8 keV count rate and the strength of the 3 keV feature did not change significantly. If a flare is the cause of the observed excess, then such a flare event must have been extremely long-lived, as we have found same 3 keV feature, at a similar strength, present in point-source and background subtracted spectra from our shorter ACIS observation of NGC 253 taken eleven days earlier (on 2000 December 16), and in the archived observations of SN 1999em (ObsID 765, taken 2000 December 16) and the QSO 3C 220.1 (ObsID 839, taken 2000 December 29). No such spectral feature is found in the XMM-Newton PV observation of NGC 253 (Summers 2001, private communication). We therefore feel confident that the 3 keV feature is not genuinely associated with NGC 253. The detection of *any* diffuse emission at energies above 2 keV is of marginal significance in any case (0.0107 ± 0.0032 count s^{-1} in the 2 – 8 keV energy band), and is best treated as an upper limit on the hard X-ray emission from the superwind.

4.2. Spatial variation in spectral properties

Prior to attempting to fit the X-ray spectrum of the diffuse emission, it is important to assess the amount of spatial variation of the spectral properties within the region used to obtain the spectrum. We wish to limit the degree to which any spectrum mixes together emission from spectrally distinct regions, either of different temperature or hidden behind different amounts of absorption.

Any spatial variation in spectral properties of the diffuse emission might also provide important clues as to the origin of the X-ray emission. For example, if the X-ray emission comes from internal shocks within the wind, then we might expect increases in characteristic temperature (or spectral hardness) to directly correlate with enhancements in X-ray surface brightness. If the X-ray emission comes from a spatially-resolved constant-pressure conductive interface (e.g. as in the Weaver et al. (1977) wind-blown-bubble model) we expect the gas temperature to decrease as the density (and surface brightness) increases.

The limiting factor that controls what range of spatial scales over which spectral variation can be investigated in such an analysis using *Chandra* is signal-to-noise per spatial bin, rather than the spatial resolution of the instrument. With arcsecond spatial resolution there is no effective “cross-talk” between spatial bins, and point sources can easily be removed without leading to significant loss of area. Given the surface brightness of the halo diffuse emission and the instrumental and X-ray backgrounds, we found that obtaining hardness ratios with any meaningful statistical certainty necessitates using spatial bins at least $30''$ -wide. This corresponds to physical scales of $\gtrsim 380$ pc at the distance of NGC 253.

4.2.1. Hardness ratio maps of the halo

Fig. 5a shows a hardness map of the diffuse emission in the northern halo, constructed using $1'$ -wide pixels. The hardness ratio is defined as $Q = (H - S)/(H + S)$, where H is the count rate in hard band and S is the count rate in the soft band. Defined in this way, the hardness ratio always lies between -1 (soft) and 1 (hard).

We use data from the 0.6–1.0 keV energy band as the hard band, and the 0.3–0.6 keV energy band

as the soft band, as the observed halo region spectrum has roughly equal number of counts in these two bands (hence maximizing the S/N in each band). A harder (higher temperature and/or more absorbed) X-ray spectrum in any region gives a positive hardness ratio and a soft spectrum a negative hardness ratio.

For the low X-ray count rates found in superwinds, hardness ratio maps do not give a statistically robust estimate of variations in hardness due to Poisson fluctuations. Fig. 5b is a hardness ratio deviation significance map, which maps the statistical significance of any deviation from the mean hardness of the diffuse emission. For each pixel i, j in the image, the hardness ratio deviation significance is $(Q_{i,j} - Q_{\text{mean}})/\sigma_{Q_{i,j}}$, where $Q_{i,j}$ is the hardness ratio at that point, $\sigma_{Q_{i,j}}$ is the uncertainty in the hardness ratio at that point, and Q_{mean} is the mean hardness of the diffuse emission. The procedure used to construct the hardness ratio and hardness ratio deviation significance maps is discussed in Appendix C. Note that the calibration problems discussed in § 2.1.5 have negligible effect on these hardness ratio studies, given the broad energy bands used.

We find only marginally-significant deviations ($\lesssim 3\sigma$) from the mean hardness ratio in the halo. These do not appear to correlate with the structure seen in the soft X-ray surface brightness map, which suggests that these hardness variations are noise. Support for this hypothesis comes from the number distribution of hardness ratio deviation significances, which is well fit with a model of Gaussian random noise (Fig. 5c). Consistent results are obtained if larger or smaller bin sizes ($2'$ or $30''$ -wide pixels) are used for the hardness ratio maps.

On angular scales of $30'' - 2'$ (~ 380 to 1500 pc) we conclude that there is no statistically significant variation in the spectral properties of the diffuse emission from the superwind.

4.2.2. Hardness ratio maps of the disk

We applied the same hardness ratio mapping technique to investigate the degree of spectral variation in the diffuse X-ray emission from the disk of the galaxy.

We used the data from the 43 ks observation in which the disk of the galaxy was placed on the

TABLE 2
SPECTRAL HARDNESS RATIOS IN THE HALO, DISK AND NUCLEAR OUTFLOW CONE

Region (1)	Count rate (2)	Q_A (3)	Q_B (4)	Q_C (5)
Northern halo	0.2092 ± 0.0053	-0.035 ± 0.018	-0.755 ± 0.025	-0.909 ± 0.034
NE halo	0.0521 ± 0.0025	$+0.002 \pm 0.037$	-0.799 ± 0.051	-0.795 ± 0.061
NW halo	0.0292 ± 0.0023	-0.018 ± 0.061	-0.633 ± 0.073	-0.827 ± 0.103
SE halo	0.0521 ± 0.0025	-0.103 ± 0.034	-0.783 ± 0.045	-1.000 ± 0.064
SW halo	0.0750 ± 0.0026	-0.018 ± 0.029	-0.752 ± 0.037	-0.888 ± 0.047
Disk	0.4527 ± 0.0073	0.188 ± 0.017	-0.615 ± 0.018	-0.832 ± 0.021
Cone (east limb)	0.0184 ± 0.0020	0.139 ± 0.074	-0.666 ± 0.088	-0.992 ± 0.163
Cone (center)	0.0084 ± 0.0019	0.284 ± 0.117	-0.689 ± 0.154	-0.994 ± 0.329
Cone (west limb)	0.0423 ± 0.0024	0.404 ± 0.053	-0.545 ± 0.051	-0.979 ± 0.082

NOTE.—Errors are quoted at 68% percent confidence. Column (1): The halo and disk regions are defined in Table 1. Cone refers to the clearly limb-brightened region of the southern nuclear outflow cone, as defined in Strickland et al. (2000) (2): Background and source-subtracted ACIS-S3 count rate (units of counts/s) in the 0.3 – 8.0 keV energy band. These count rates have *not* been corrected for the area lost due to point source removal. (3): Hardness ratio $Q=(H-S)/(H+S)$, where H is the count rate in the 0.6 – 1.0 keV energy band and S is the count rate in the 0.3 – 0.6 keV energy band. (4): Hardness ratio using count rates in the 1.0 – 2.0 keV (H) and 0.3 – 1.0 keV (S) energy bands. (5): Hardness ratio using count rates in the 2.0 – 8.0 keV (H) and 0.3 – 2.0 keV (S) energy bands.

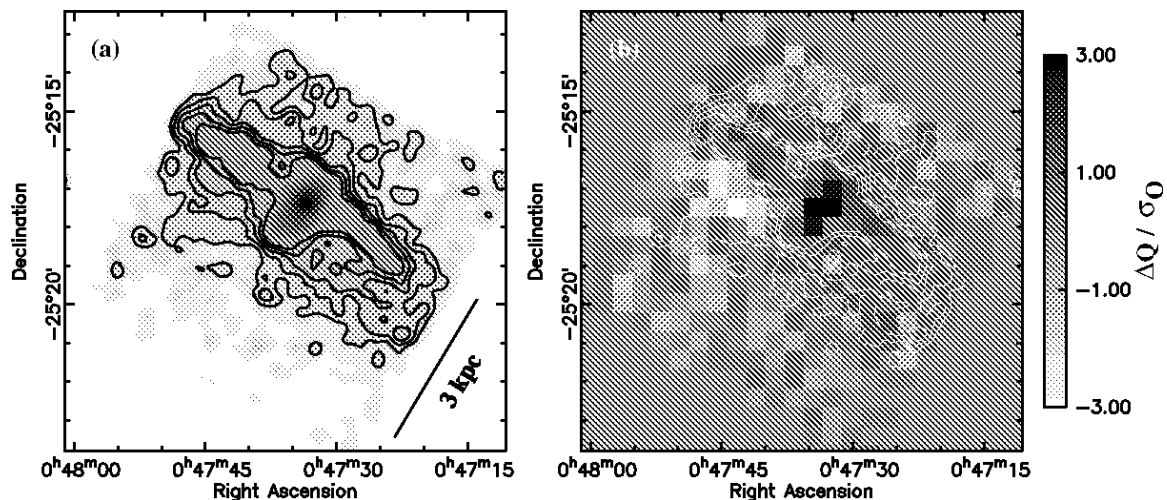


Fig. 6.— (a) Chandra ACIS-S2 0.3 – 2.0 keV image of the diffuse X-ray emission from the disk of NGC 253, along with the inner halo to the SE and NW of the disk, smoothed with a 20'' FWHM Gaussian mask. Point sources and background emission have been subtracted from the data. Contours are shown at signal-to-noise ratios of 2, 3, 4, 5 & 6 above the background within a 20''-diameter aperture. The grey scale image is shown on a logarithmic intensity scale between 10^{-7} to 3×10^{-4} counts s^{-1} arcsec $^{-2}$. (b) The diffuse emission hardness ratio deviation significance map. White contours correspond to those shown in panel (a). The only regions that deviate significantly from the mean spectral hardness are the nuclear outflow cone (spectrally harder than the disk) and a small region near the base of the south eastern plume of the superwind (spectrally softer than the rest of the diffuse X-ray emission from the disk). The pixel scale is 30''.

front-illuminated S2 chip. This provides approximately twice the total number of counts as the

shorter observation with the disk in the S3 chip, and has the added advantage that the spatial cov-

erage of the S2 chip extends a few kpc into the southern halo, partially covering the south eastern spur of the superwind seen in Fig. 1.

As with the hardness maps of the halo, we used 0.3 – 0.6 keV and 0.6 – 1.0 keV energy bands, having subtracted both point sources and background from the data. A point source-subtracted image of the diffuse emission is shown along with the hardness ratio deviation significance map in Fig. 6.

Only two regions show hardness ratios that deviate significantly from the mean spectral hardness of the diffuse disk emission. Diffuse emission from the central ~ 1 kpc (comprising the obscured starburst region, the southern nuclear outflow cone and the heavily absorbed northern outflow cone) appears systematically harder than the rest of the disk. Note that this region had been excluded when initially calculating the mean spectral hardness of the disk. To the east of the nucleus, somewhat away from the brightest emission from the disk, is a $\sim 3' \times 1.5'$ region that is significantly softer than the average disk emission. Pietsch et al. (2001) noted that this region [which they call NE(S)] appeared spectrally soft in the *XMM-Newton* EPIC PN data, and suggested it came from less absorbed gas above the disk of the galaxy. In the *Chandra* data this region seems to lie at the base of the base of the south eastern plume of H α and soft X-ray emission (compare Fig. 6 with Figs. 1 & 9), possibly indicating an association with the superwind.

4.2.3. Spectral variation over larger spatial scales

We searched for spectral variation in the halo diffuse emission between the 4.2'-square quadrants that make up the northern halo region. These quadrants cover a range in diffuse X-ray surface brightness, from the faint NW region away from the X-ray arc, through the moderately brighter SE and NE regions to the brightest diffuse emission in the SW region. If there is any significant variation in the spectral properties of the diffuse emission over ~ 3 kpc scales, then this should be apparent comparing the diffuse emission spectra from these four regions.

We found only weak differences between the regions in any of the hardness ratios we considered (see Table 2), none of which are statistically significant at more than the 2σ level. Based on Fig. 7

this limits variations in characteristic temperature in the halo to $\lesssim 50\%$, or changes in hydrogen column of $\lesssim 0.5$ dex.

4.3. Spectral fitting

Given the lack of significant spatial variation in the spectral properties of the diffuse X-ray emission over the halo region, we have chosen to fit spectral models to the ACIS spectrum of the entire halo region.

The count rate in the diffuse spectrum at energies above 2 keV is only marginally significant, and as discussed previously the detected counts are likely to be due to low-level systematic problems with the background subtraction. For this reason we choose to fit the data only in the energy range 0.3 – 2.5 keV to avoid biasing the fits. Experiments of fitting the data using a wider energy range give similar and consistent results, in several cases with lower values of reduced χ^2 due to the addition of data points with very large uncertainties. Within the 0.3 – 2.5 keV energy range the background and source subtracted count rate from the diffuse halo emission is 0.2014 ± 0.0037 counts per second (a total of 7973 ± 146 counts over 39588 seconds).

4.3.1. Spectral models

We considered a variety of models that might reasonably be expected to represent the thermal X-ray emission from the hot gas in superwinds. The standard hot plasma models used to fit the soft thermal component in superwinds assume collisional ionization equilibrium (CIE). We have used four of the currently available CIE hot plasma codes: MEKAL (Mewe, Kaastra & Liedahl 1995), APEC (Smith et al. 2001), the Raymond-Smith code (Raymond & Smith 1977) and the EQUIL (Borkowski, Lyerly & Reynolds 2001) code. When combined with a photoelectric absorption model (Morrison & McCammon 1983) a hot plasma model is parameterized in terms of equivalent hydrogen column N_{H} , gas thermal temperature kT , metal abundances relative to Solar⁹ and an overall normalization which depends

⁹Note that abundances within XSPEC are based on Anders & Grevesse (1989), which over-estimates the Fe abundance by 0.17 dex compared to more recent estimates (e.g. Grevesse & Noels (1993)).

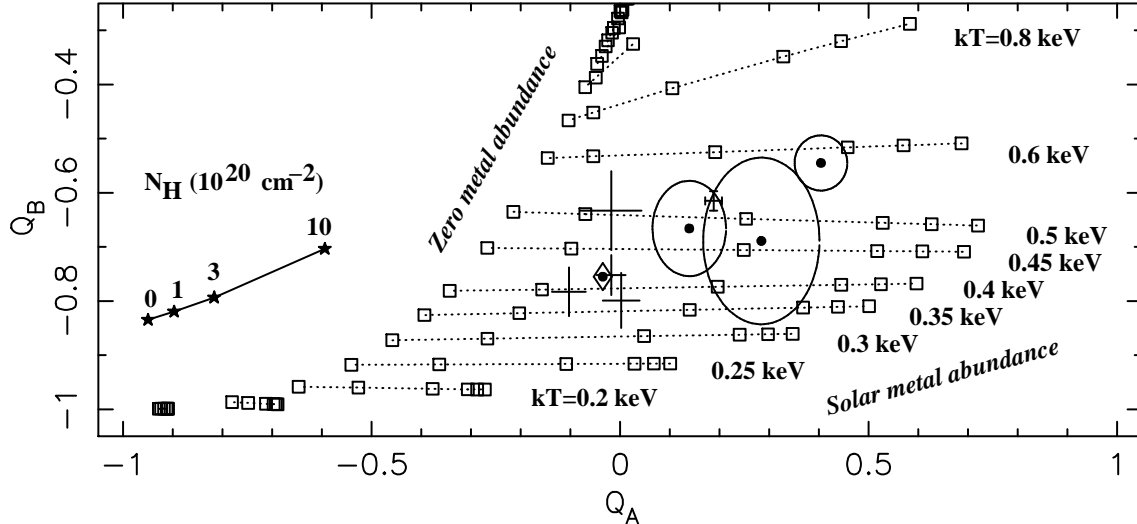


Fig. 7.— A hardness ratio Q_a vs. hardness ratio Q_B plot, showing the observed hardness ratios of the northern halo diffuse emission (diamond), the four separate quadrants of the northern halo (crosses), the diffuse disk emission (barred cross) and the center, east and west limbs of the southern nuclear outflow cone (ellipses). The hardness ratios Q_A and Q_B are defined in Table. 2. Theoretical hardness ratios are shown for an *unabsorbed* single phase hot plasma with $kT = 0.1, 0.15, 0.2, 0.25, 0.3, 0.35, 0.4, 0.45, 0.5, 0.6, 0.8, 1.0$ and 1.25 keV, $10 \times 10^{20} \text{ cm}^{-2}$, where the open squares represent $Z = 0, 0.02, 0.1, 0.3, 0.5$ and $1 \times Z_\odot$ moving from left to right. The starred points on the left of the plot show the degree to which these hardness ratios change depending on the foreground hydrogen column density. The relative softness of all the diffuse emission regions in ratio Q_A forces the fits to give low metal abundances when using single phase spectral models. Error bars are 1σ confidence levels.

on the emission integral $EI = \int n_e n_H dV$. Non-ionization equilibrium (NIE) models, using the code developed by Borkowski, Lyerly & Reynolds (2001), are further characterized by an ionization timescale defined as the product of the electron density and the age $n_e \tau$. The NEI model represents initially cold neutral gas which has been suddenly heated, in which the ionization state of the ions is lower than in a CIE plasma of the same kinetic (electron) temperature. Other non-ionization equilibrium models with different ionization histories (e.g. cooling gas more ionized than a same-temperature CIE plasma), such the GNEI and PSHOCK models in XSPEC, give similar or worse fits to the spectra than the NEI model does. For the sake of brevity we will not discuss these other NIE models again. Higher resolution spectroscopy will be needed to robustly constrain the ionization state and history of the X-ray emitting gas in superwinds. Our primary interest in the results of the NIE models is whether ionization

effects significantly alter the fitted metal abundances.

These spectra only constrain the abundances of those elements that produce strong line emission in the *Chandra* energy band, and which produce lines or line complexes at energies not covered by emission from other elements that produce stronger line emission. We have calculated the fraction of emission due to lines of each element for a range of plasma temperatures using the MEKAL code. Oxygen and iron abundances are likely to be the best-constrained in ACIS spectra of soft thermal X-ray emission due to their intensity¹⁰, followed by magnesium and silicon abundances due to their clear separation in energy space from other spectral features. In principle element abundances

¹⁰For a plasma with Solar element abundances oxygen (iron) provides 58% (14%) of the ACIS-S 0.3 – 2.5 keV energy band count rate from a $kT = 0.2$ keV, $N_H = 3 \times 10^{20} \text{ cm}^{-2}$ plasma, and 13% (61%) of the emission from a $kT = 0.5$ keV plasma with the same hydrogen column.

of C, N, Ne & S can also be constrained, although the low energy of the main C, N and S lines, and for Ne confusion with the strong emission from Fe, makes abundances determinations more difficult. Confusion with Fe is a major problem for determining Ni abundances. We can not realistically constrain Na, Al, Ar & Ca abundances given the low emissivities and line confusion. For the purposes of the spectral fitting we have fixed the relative abundances of Na, Al, Ca and Ni to be equal to that of Fe (*i.e.* $[X/H] = [Fe/H]$ where X is the element in question), as these are all refractory elements and depletion onto dust grains may be significant in the X-ray emitting plasma. The Ar relative abundance was made equal to the Ne abundance.

4.3.2. Single phase spectral models

Single temperature spectral models of the type discussed in the previous section all provided statistically unacceptable fits to the halo spectrum. Reduced chi-squared values in the range $\chi^2_{\nu} = 1.22$ to 1.99 were obtained for between 77 and 85 degrees of freedom, depending on which model was used.

Fitted temperatures were typically $kT \sim 0.4$ keV, the extremes being 0.25 and 0.69 keV. Best fit metal abundances were always extremely low, typically $Z = 0.02 \pm 0.02 Z_{\odot}$. Fitted oxygen and iron abundances were $Z_O \sim 0.05 Z_{O,\odot}$ (typical 90% uncertainty $\lesssim 0.06 Z_{\odot}$) and $Z_{Fe} \sim 0.03 Z_{Fe,\odot}$ (typical 90% uncertainty $\lesssim 0.07 Z_{\odot}$). Note that this is very similar to the temperature and abundances one would infer from a simple hardness ratio analysis (see Fig. 7). The simple explanation is that the fitting process must match the broad band spectral shape of the halo spectrum. Direct diagnostics of the temperature of the plasma (e.g. using flux ratios of the hydrogen to helium-like oxygen line complexes), or of the metal abundance (e.g. the apparent equivalent width of line emission above the continuum) play only a secondary role in constraining the fitted parameters. Metal line equivalent widths are extremely difficult to measure from ACIS resolution spectra directly, as the continuum is buried under the merged blend of line emission¹¹.

The different CIE hot plasma models (MEKAL, APEC, EQUIL and the Raymond Smith code) gave results consistent with each other in most cases (the admittedly older-vintage Raymond Smith code gave the statistically worst fits). If there are significant problems with the atomic physics used in these codes then this affects all the codes equally.

Using non-ionization equilibrium models does not lead to significantly different metal abundances than the CIE models, so it does not appear that the apparently low abundances are simply a consequence of unusual ionization states in a single phase gas.

4.3.3. Multi-phase spectral model fits to the disk and halo

The strongest features in the halo spectrum are emission at $E \sim 0.55$ and 0.63 keV (Fig. 8), which are of roughly equal strength. Correcting for the ~ 20 eV error in the energy scale, these match up well with the OVII and OVIII line complexes. If both features come from the same gas phase, and collisional ionization equilibrium holds, then the approximately equal strength of these two features constrains the temperature to be $kT \sim 0.25$ keV. The ratio of the OVII line complex to OVIII line complex count rates is a strong function of temperature (at $kT = 0.15$ keV the ratio is ~ 5 , at 0.2 keV the ratio is ~ 2 , at 0.25 keV the ratio is ~ 1 , at 0.3 keV the ratio is ~ 0.5 and at 0.4 keV the ratio is ~ 0.25).

This temperature is lower than the best-fitting temperature in the single phase spectral models. Taken at face value, this forces us to consider two phase or multi-phase spectral models in order to obtain equal strength OVII and OVIII emission in a spectrum that is harder than a $kT = 0.25$ keV plasma. This argument should be robust against calibration uncertainties, as it is not based on the absolute intensities or detailed shape or equivalent widths of the two features. Uncertainties in the effective area of the instrument are also unlikely to be significant given the close proximity of the two features in energy space.

A multi-phase model can potentially explain the observed spectra without requiring such low

¹¹Only ~ 5 to 10% of the counts from a Solar abundance plasma are from the continuum for gas temperatures $0.1 \lesssim$

$kT \lesssim 1$ keV, and line emission covers the continuum at almost all energies below 2 keV.

TABLE 3

MULTI-COMPONENT SPECTRAL MODEL FITS TO THE DIFFUSE HALO AND DISK EMISSION

Model (1)	N_{H} (2)	kT_1 or Γ (3)	kT_2 (4)	$\log(n_e\tau)_1$ (5)	$\log(n_e\tau)_2$ (6)	α_{DEM} (7)	$FWHM$ (8)	K_1 (9)	K_2 (10)	ΔE (11)	χ^2_{ν} (χ^2/ν) (12)
Northern halo spectral fits											
2Tvmekal	$6.1^{+8.0}_{-1.5}$	$0.24^{+0.07}_{-0.04}$	$> 0.4^{\text{a}}$	$34.16^{+88.79}_{-25.37}$	$1.66^{+1.57}_{-1.25}$	-38^{+21}_{-24}	1.19 (91.8/77)
2Tvapec	$5.3^{+8.3}_{-2.1}$	$0.24^{+0.03}_{-0.04}$	$0.71^{+3.18}_{-0.36}$	$40.96^{+95.12}_{-30.47}$	$4.79^{+11.39}_{-4.33}$	-27^{+25}_{-16}	1.11 (85.3/77)
2Tvnei	$5.0^{+7.4}_{-3.0}$	$0.33^{+0.18}_{-0.33}$	14.2^{b}	$11.17^{+5.83}_{-0.65}$	$21.53^{+17.80}_{-11.83}$	$0.87^{+1.99}_{-0.87}$	-34^{+25}_{-19}	1.23 (93.7/76)
2Ivnei	$2.1^{+8.2}_{-1.8}$	$0.70^{+0.65}_{-0.35}$...	$9.88^{+1.81}_{-9.88}$	$10.99^{+0.61}_{-0.49}$	$1.06^{+2.02}_{-1.06}$	$4.23^{+13.48}_{-3.20}$	-29^{+25}_{-15}	1.13 (86.1/76)
GTvmekal	$5.5^{+7.0}_{-2.8}$	$0.26^{+0.10}_{-0.19}$	$0.446^{+1.386}_{-0.445}$	$31.61^{+63.18}_{-26.21}$...	-32^{+24}_{-22}	1.29 (100.4/78)
PLTvmekal	$5.7^{+4.8}_{-2.8}$	$0.20^{+0.09}_{-0.04}$	$> 18.1^{\text{a}}$	$-2.42^{+2.28}_{-7.40}$...	$31.21^{+31.46}_{-20.71}$...	-33^{+22}_{-25}	1.25 (96.1/77)
PL+vapec	$6.4^{+3.4}_{-3.6}$	$3.3^{+0.5}_{-2.9}$	$0.24^{+0.04}_{-0.03}$	$7.83^{+17.20}_{-2.72}$	$3.72^{+248.2}_{-3.17}$	-28^{+28}_{-20}	1.16 (89.0/77)
Disk diffuse emission spectral fits											
2Tvmekal	$4.4^{+2.7}_{-2.1}$	$0.17^{+0.12}_{-0.10}$	$0.57^{+0.06}_{-0.08}$	$5.98^{+40.27}_{-4.41}$	$21.21^{+1.36}_{-9.72}$	-2^{+21}_{-10}	1.39 (128.3/92)
2Tvapec	$4.7^{+4.2}_{-2.4}$	$0.17^{+0.07}_{-0.11}$	$0.56^{+0.13}_{-0.06}$	$8.25^{+55.18}_{-3.20}$	$32.37^{+22.53}_{-18.47}$	-1^{+21}_{-7}	1.34 (123.6/92)
2Ivnei	$2.8^{+4.1}_{-2.4}$	$1.24^{+2.14}_{-0.74}$...	$> 9.60^{\text{a}}$	$> 10.10^{\text{a}}$	$4.65^{+17.01}_{-3.07}$	$3.97^{+19.74}_{-3.32}$	-5^{+15}_{-17}	1.36 (124.1/91)
2Tvnei	$2.9^{+3.3}_{-1.8}$	$0.49^{+0.24}_{-0.16}$	$> 0.60^{\text{a}}$	$10.54^{+0.29}_{-0.11}$	$11.16^{+9.24}_{-5.96}$	$5.39^{+2.59}_{-3.34}$	-5^{+16}_{-16}	1.21 (109.9/91)
GTvmekal	$5.2^{+3.3}_{-2.8}$	$0.30^{+0.21}_{-0.20}$	$0.76^{+0.56}_{-0.34}$	$41.31^{+201.81}_{-28.81}$...	-3^{+11}_{-12}	1.44 (133.8/93)
PLTvmekal	$5.0^{+3.6}_{-2.6}$	$0.08^{+0.17}_{-0.08}$	$0.82^{+2.82}_{-0.28}$	$0.51^{+1.16}_{-2.48}$...	$36.95^{+50.97}_{-19.67}$...	-3^{+22}_{-12}	1.41 (129.9/92)
PL+vapec	$6.1^{+4.0}_{-4.1}$	$2.1^{+0.8}_{-1.6}$	$0.25^{+0.11}_{-0.05}$	$17.05^{+9.66}_{-10.15}$	$3.71^{+73.12}_{-3.64}$	-5^{+18}_{-10}	1.38 (126.8/92)

NOTE.—All errors are 90% confidence for a number of interesting parameters equal to the number of free parameters in the model (13, 14 or 15 free parameters depending on the model). Best-fit element abundances are given in Table 4. Column (1): XSPEC model name. Variable metal abundance hot plasma codes that assume collisional ionization equilibrium are vmekal & vapec, while vnei is a variable abundance non-ionization equilibrium plasma model. A prefix of 2T or 2I denotes that the model is a two temperature or two ionization timescale model, while GT and PLT refer to power law or Gaussian distributions of emission integral as a function of temperature. The PL+vapec model is a two component power law plus vapec thermal plasma model. See text for details. Column (2): Hydrogen column density in units of 10^{20} cm^{-2} . Columns (3) & (4): Gas temperatures in keV. For the 2T models column (3) is the temperature of the first component, and column (4) the temperature of the second component. For the PLT model (3) is the minimum temperature and (4) the maximum temperature over which the power law in emission integral holds. For the GT model (3) is the central temperature of the Gaussian emission integral distribution. For the PL+vapec model column (3) is the photon index of the power law Γ , where the flux $f(E) \propto E^{-\Gamma}$. Columns (5) & (6): Logarithm of the ionization timescale (cgs units) in the 2Tvnei and 2Ivnei models. Column (7): The slope α of the emission integral distribution in the PLT model, where $EI(T) \propto T^\alpha$. Column (8): Full width at half maximum (dex) of the Gaussian distribution in X-ray emission integral used in the GT model. Note that the distribution is Gaussian in $\log T$. Columns (9) & (10): Model component normalizations, where $K = 10^{-10} EI/4\pi D^2$. D is the distance to the source, and the emission integral $EI = \int n_e n_{\text{H}} dV$ is the volume integral of the electron and hydrogen number densities. For the PL+vapec model column (9) is the power law normalization in units of $10^5 \text{ photons s}^{-1} \text{ keV}^{-1} \text{ cm}^{-2}$ at $E = 1 \text{ keV}$. Column (11): Best-fit energy shift applied to the spectral response in eV. Column (12): Fit statistics: the reduced chi-squared (χ^2_{ν}), the value of χ^2 and the number of degrees of freedom.

^aAt 90% confidence only a lower limit on the value of this parameter could be obtained.

^bAt 90% confidence this parameter is unconstrained.

^cParameter fixed at this value during fitting.

TABLE 4
METAL ABUNDANCES FROM THE MULTI-COMPONENT SPECTRAL MODELS

Model (1)	C (2)	N (3)	O (4)	Ne, Ar (5)	Mg (6)	Si (7)	S (8)	Fe, Na, Al, Ca (9)
Northern halo spectral fits								
2Tvmekeal	$0.168^{+1.357}_{-0.168}$	$0.000^{+0.756}_{-0.000}$	$0.042^{+0.109}_{-0.021}$	$0.097^{+0.178}_{-0.067}$	$0.306^{+0.965}_{-0.306}$	$0.204^{+3.242}_{-0.204}$	$0.000^{+0.316}_{-0.000}$	$0.053^{+0.153}_{-0.032}$
2Tvapec	$0.226^{+1.634}_{-0.0226}$	$0.000^{+0.689}_{-0.000}$	$0.038^{+0.319}_{-0.023}$	$0.037^{+0.147}_{-0.037}$	$0.226^{+2.086}_{-0.226}$	$0.252^{+1.718}_{-0.252}$	$0.000^{+0.440}_{-0.000}$	$0.050^{+0.217}_{-0.032}$
2Tvnei	$0.397^{+4.262}_{-0.397}$	$0.000^{+0.581}_{-0.000}$	$0.026^{+0.227}_{-0.015}$	0.056^a	$0.188^{+2.685}_{-0.188}$	$0.444^{+8.161}_{-0.444}$	$0.000^{+1.209}_{-0.000}$	$0.037^{+0.115}_{-0.024}$
2lvnei	$0.212^{+2.443}_{-0.212}$	$0.33^{+19.34}_{-0.33}$	$0.092^{+0.825}_{-0.060}$	$0.026^{+0.445}_{-0.026}$	$0.163^{+0.359}_{-0.163}$	$0.125^{+2.098}_{-0.125}$	$0.000^{+0.000}_{-7.370}$	$0.107^{+0.294}_{-0.107}$
GTvmekeal	$0.190^{+7.043}_{-0.190}$	$0.000^{+2.185}_{-0.000}$	$0.064^{+0.475}_{-0.032}$	$0.064^{+0.165}_{-0.064}$	$0.179^{+0.500}_{-0.179}$	$0.227^{+1.119}_{-0.227}$	$0.000^{+0.670}_{-0.000}$	$0.032^{+0.221}_{-0.017}$
PLTvmekeal	$0.228^{+1.178}_{-0.228}$	$0.000^{+0.536}_{-0.000}$	$0.057^{+0.114}_{-0.030}$	$0.075^{+0.179}_{-0.075}$	$0.215^{+0.332}_{-0.215}$	$0.299^{+2.036}_{-0.299}$	$0.000^{+0.446}_{-0.000}$	$0.043^{+0.110}_{-0.025}$
PL+vapec	$2.2^{+16.3}_{-2.2}$	$0.0^{+4.2}_{-0.0}$	$0.45^{+0.35}_{-0.22}$	$0.85^{+0.94}_{-0.66}$	3.3^a	4.3^a	$0.0^{+11.7}_{-0.0}$	$0.81^{+0.45}_{-0.69}$
Disk diffuse emission spectral fits								
2Tvmekeal	$0.000^{+1.437}_{-0.000}$	$0.019^{+1.076}_{-0.019}$	$0.212^{+0.476}_{-0.152}$	$0.045^{+0.180}_{-0.045}$	$0.150^{+0.476}_{-0.150}$	$0.340^{+0.618}_{-0.170}$	$1.072^{+2.454}_{-1.072}$	$0.072^{+0.063}_{-0.035}$
2Tvapec	$0.000^{+1.033}_{-0.000}$	$0.304^{+1.923}_{-0.304}$	$0.152^{+0.463}_{-0.128}$	$0.063^{+0.292}_{-0.063}$	$0.096^{+0.471}_{-0.096}$	$0.275^{+0.978}_{-0.263}$	$1.061^{+3.929}_{-1.061}$	$0.049^{+0.074}_{-0.025}$
2lvnei	$0.000^{+0.085}_{-0.000}$	$0.127^{+0.160}_{-0.000}$	$0.042^{+0.059}_{-0.023}$	$0.019^{+0.071}_{-0.019}$	$0.105^{+0.187}_{-0.105}$	$0.264^{+0.710}_{-0.264}$	$0.686^{+0.713}_{-0.686}$	$0.141^{+0.222}_{-0.098}$
2Tvnei	$0.019^{+0.352}_{-0.019}$	$0.071^{+0.202}_{-0.070}$	$0.032^{+0.028}_{-0.016}$	$0.037^{+0.094}_{-0.037}$	$0.097^{+0.260}_{-0.097}$	$0.212^{+0.411}_{-0.212}$	$0.239^{+0.761}_{-0.239}$	$0.116^{+0.201}_{-0.071}$
GTvmekeal	$0.000^{+1.170}_{-0.000}$	$0.021^{+1.397}_{-0.021}$	$0.102^{+0.340}_{-0.048}$	$0.061^{+0.184}_{-0.061}$	$0.194^{+0.574}_{-0.194}$	$0.395^{+0.986}_{-0.395}$	$0.410^{+1.009}_{-0.410}$	$0.088^{+0.202}_{-0.039}$
PLTvmekeal	$0.000^{+0.587}_{-0.000}$	$0.000^{+1.071}_{-0.000}$	$0.126^{+0.239}_{-0.082}$	$0.017^{+0.182}_{-0.017}$	$0.180^{+0.503}_{-0.180}$	$0.361^{+0.690}_{-0.350}$	$0.601^{+1.046}_{-0.601}$	$0.081^{+0.078}_{-0.039}$
PL+vapec	$0.0^{+18.8}_{-0.0}$	$2.6^{+39.6}_{-2.6}$	$0.73^{+9.52}_{-0.64}$	$2.4^{+18.7}_{-2.0}$	4.4^a	14.1^a	$4.2^{+34.8}_{-4.2}$	$2.5^{+13.7}_{-2.1}$

NOTE.—Abundances are relative to Anders & Grevesse (1989) Solar abundance. All errors are 90% confidence for a number of interesting parameters equal to the number of free parameters in the model. The relative argon abundance is assumed to be equal to the neon relative abundance. The relative abundances of sodium, aluminum, calcium and nickel are assumed to be equal to the relative iron abundance. Model names are the same as used in Table 3.

^aAt 90% confidence this parameter is unconstrained within the range 0 to 50 Z_{\odot} .

abundances. Multi-phase or multi-component spectral models successfully removed the need to invoke extremely low abundances in the *ROSAT* and *ASCA* spectra of entire starburst galaxies (Dahlem, Weaver & Heckman (1998); Weaver, Heckman & Dahlem (2000); Dahlem et al. (2000)). One phase with strong OVII but weak OVIII emission, along with another phase of higher temperature having weak OVII and strong OVIII, might look like a $kT \sim 0.25$ keV plasma with lower oxygen abundance as the two continuum components would reduce the equivalent width of each oxygen line complex.

We fit a variety of two temperature CIE and NIE variable metallicity spectral models to the halo spectrum, using the MEKAL, APEC and NEI plasma codes. For the multi-phase NIE models we considered cases where two components of different temperature had the same ionization timescale (2Tvnei), or two components of different ionization timescale had the same temperature (the 2Ivnei model). We also considered two slightly more complex phase distributions, motivated by the hydrodynamical models of Strickland & Stevens (2000) which predict that the X-ray emission integral as a function of temperature is approximately a power law. In the PLT model the X-ray emission integral is proportional to a power law function of the gas temperature between a minimum and maximum temperature, *i.e.* $EI(T) \propto T^\alpha$. We also considered a Gaussian distribution in emission integral as a function of (log) temperature, $EI(T) \propto \exp(-4 \ln 2 \times [\{\log T - \log T_{\text{cent}}\}/FWHM]^2)$, where the Gaussian is centered at temperature T_{cent} . In all cases we assumed that the multiple phases in the model had the same metal abundance. The statistical quality of the data, along with the current calibration uncertainties, do not justify multi-component fits where each component has a different metallicity. The results of these fits are presented in Tables 3 & 4.

Unfortunately, and somewhat to our surprise, *multi-phase models do not solve the low metal abundance problem* in the halo. Although the fits are statistically superior to those using single temperature models, they remain somewhat poor statistically-speaking. The best-fitting models (shown in Fig. 8), the two temperature APEC and the two ionization timescale NEI models have

reduced chi-squared values of 1.11 and 1.13 respectively. Such poor values of reduced chi-squared would only occur $\sim 20\%$ of the time if the models are accurately physical representations of the emitting plasma.

The best-fit metal abundances are always extremely low, irrespective of which model was used. In particular the best-constrained elemental abundances, those of oxygen and iron, are consistently in the range 0.03 to 0.09 and 0.03 to 0.10 times Solar abundance respectively. Admittedly the 90% confidence regions for the oxygen abundance are moderately large, but given the systematically, unbelievably, low best-fit abundances we have little confidence in the statistical confidence regions.

Can depletion onto dust explain the apparently low gas-phase abundances? Physically it is quite possible that the X-ray emitting gas may contain a significant dust fraction. There is a wide range of evidence pointing to dusty material in superwinds (Phillips (1993); Alton, Davies & Bianchi (1999); Heckman et al. (2000)). It is striking that FIR images of NGC 253 made by *ISOPHOT* at 60, 100 and 180 μm show enhanced dust emission along the X-ray-emitting arcs seen in Fig. 1 (Radovich, Kahapää & Lemke 2001). Invoking depletion onto dust *does not* explain the fitted abundances, where abundances of both refractory and non-refractory elements are extremely low. Although iron is heavily depleted onto dust in the warm ISM (by factors of up to a hundred), oxygen is only weakly depleted (Savage & Sembach 1996).

Extremely low gas phase oxygen abundances are difficult to explain physically, unless the X-ray emitting gas is relatively unenriched material in the halo of NGC 253. For example some Galactic high velocity clouds have relatively low oxygen abundances, $Z_O \sim 0.1Z_{O,\odot}$, while other halo clouds possibly of Galactic origin have approximately Solar oxygen abundance (Richter et al. 2001).

4.3.4. Spectral fits to the disk diffuse emission

The hot gas in the disk of NGC 253 can not be primordial, and therefore should have oxygen abundances within a factor few of Solar. If multi-phase spectral fits to the diffuse emission from the disk also give strongly sub-Solar oxygen abundances then we will have good evidence that the

X-ray determined abundances can not be trusted.

The disk diffuse spectrum was obtained from the 13ks Chandra observation with the disk placed on the S3 chip. Based on the hardness ratio study we excluded diffuse emission from starburst region and nuclear outflow cones, in addition to emission from point sources. We included data from the spectrally soft region to the east of the nucleus (see § 4.2.2). As the total flux from this region is only a small fraction of the diffuse flux from the disk this will not significantly complicate the spectrum of the disk.

We applied the same multi-phase spectral models to the disk diffuse emission as had been used on the halo diffuse emission, the results of which are shown for reasons of completeness in Tables 3 & 4. The most important result worth noting is that both best-fit oxygen and iron abundances are again extremely low in all the multi-phase models.

This makes untenable the argument that low X-ray-derived oxygen abundances arise from relatively primordial material suggested above (invoked independently by Xia et al. (2001) in the case of the extended X-ray emission from the Ultra-luminous IR galaxy Mrk 273).

4.3.5. *A mix of thermal and non-thermal X-ray emission?*

The only method we have found to obtain reasonably high oxygen and iron abundances is by adding a non-thermal component to the spectral model (the PL+vapec model in Tables 3 & 4). The thermal component provides the observed line emission, while the non-thermal component accounts for much of the continuum.

Non-thermal radio emission is seen within the haloes of starburst galaxies such as M82 and NGC 4631 (Ekers & Sancisi (1977); Seaquist & Odgaard (1991)), including NGC 253 (Carilli et al. 1992), and is thought to be synchrotron emission from cosmic ray (CR) electrons that arise within the disk (and are advected out within the superwind), or are accelerated locally in internal wind shocks.

The modeled non-thermal component represents a relatively fixed fraction of the total emission at most energies, and only clearly dominates the emission at energies $E > 1.5$ keV. The soft X-ray images presented in Figs. 3 & 1 therefore

represent a reasonable approximation to the spatial distribution of the hypothesized non-thermal component, which we might expect to look similar to the non-thermal radio emission. An overlay of the soft X-ray *ROSAT* PSPC image over the radio emission is presented in Pietsch et al. (2000). The north-eastern and south-eastern arcs of X-ray emission seen by the PSPC do match up to relatively distinct features in the 330 Mhz radio emission — the “prominence” and the “spur” respectively of Carilli et al. (1992). Nevertheless, in general the radio emission is dissimilar to the X-ray emission, extending to larger galactocentric radio along the plane of the galaxy and within the lower halo immediately above the disk, at the same radio surface brightness as within the X-ray-bright regions of the halo.

Given general lack of similarity between X-ray and radio emission, along with the *Chandra* calibration uncertainties and the relatively poorly constrained parameters of the fitted spectral model, we do not believe mixed thermal plus non-thermal X-ray emission models currently provide a likely solution to the metal abundance problem. Mixed thermal and non-thermal X-ray emission is a possibility worth bearing in mind for the future, and requires more theoretical work to explore the physical feasibility of generating relatively bright synchrotron or IC X-ray emission.

4.3.6. *A summary of the abundance puzzle*

We note low X-ray-derived metal abundances appear to be a common feature in *Chandra* ACIS spectra of the extended diffuse emission in starbursting galaxies (e.g. NGC 4631 (Wang et al. 2001), Mrk 273 (Xia et al. 2001)), in addition to the longer standing findings from *ROSAT* & *ASCA*. ACIS spectra of objects that are not starbursts do not give such low best-fit element abundances¹².

Neither dust depletion, nor naturally low abundance material, nor fitting problems due to thermal emission from multi-phase gas appear to solve this problem. Calibration problems are a likely cause of the moderately high best-fit χ^2 values,

¹²Kastner, Vrtilik & Soker (2001) report near-solar O & Ne abundances, and super-Solar He, C, N, Mg & Si in a *Chandra* ACIS-S study of the diffuse X-ray emission from the planetary nebula NGC 7027. Hughes et al. (2000) find super-Solar S and Si abundances in the SNR Cassiopeia A.

but we do not believe that they are responsible for the factor ~ 20 lower-than-Solar oxygen abundances found in spectra of starbursts.

A mixed thermal plus non-thermal emission model gives more normal abundances in the halo and the disk gas. Although mixed thermal and non-thermal emission is a physically possible solution to the metal abundance problem, it requires something of a spectral conspiracy to so effectively hide a non-thermal spectrum under some thermal emission in the both the halo and the disk.

The observed ACIS spectra of both the halo and the disk look empirically like emission from low metal abundance hot plasmas. Given the line features in the spectra there is no doubt that there is some form of thermal plasma in both the halo and the disk. The limited number of spectral diagnostics that can be applied to the spectra appear consistent with each other. Physically the low abundances are unreasonable, and we are forced to conclude that we do not understand in detail the X-ray spectra of diffuse emission from star-forming galaxies. The problem of X-ray-derived metal abundances in starbursts uncovered by *ROSAT* and *ASCA* is not yet solved, and will require an imaging spectroscope with the spectroscopic resolution sufficient to robustly measure true line equivalent widths *and* the spectral shape of the continuum. We continue to urge readers to treat with caution any claims made on the basis of X-ray derived metal abundances in star-forming galaxies.

4.4. Physical properties of the X-ray-emitting plasma

4.4.1. The soft thermal emission

All spectral models give very similar values for the X-ray flux in the 0.3 – 2.0 keV energy band, $f_X \approx 5.0 \times 10^{-13} \text{ erg s}^{-1} \text{ cm}^{-2}$. This value is relatively robust, as it is closely related to the directly observed count rate. Absorption-corrected fluxes are more model-dependent, and also more uncertain due to both statistical and systematic calibration uncertainties that affect the best-fit hydrogen column (see § 2.1.5). The 2Tvapec model absorption corrected 0.3 – 2.0 keV X-ray flux for the northern halo is $f_X = 7.9 \times 10^{-13} \text{ erg s}^{-1} \text{ cm}^{-2}$ ($^{+210\%}_{-64\%}$), while the absorption-corrected flux in the 2Ivnei model is $f_X = 6.0 \times 10^{-13} \text{ erg s}^{-1} \text{ cm}^{-2}$

($^{+258\%}_{-64\%}$). Errors are based on 90% confidence regions for each model’s normalization. Adopting the latter estimate yields a total X-ray luminosity of $4.9 \times 10^{38} \text{ erg s}^{-1}$ for the superwind in the northern halo region

Plasma properties such as densities, masses and energy content are much more uncertain. *The following estimates are useful as order-of-magnitude estimates only.* We have used the total emission integral from the 2Tvapec model, $EI = 3.7 \times 10^{62} \text{ cm}^{-3}$, and a mean temperature of $T \sim 3 \times 10^6 \text{ K}$ in the following estimates. Note that the 2Ivnei model and the thermal component in the PL+vapec model give total thermal plasma emission integrals one order of magnitude lower, which would reduce all plasma properties below (except the mass cooling rate) by a factor ~ 3 .

The unknown volume filling factor η_X of the X-ray emitting gas enters into calculations of the electron number density based on the model-derived emission integral $EI = n_e n_H \eta_X V$. Possible values of η_X lie in the range 10^{-3} to 1.

As we do not believe the best-fit metal abundances, we explicitly include the scaling factor $\mathcal{R} = 0.03/Z_{\text{O,true}}$ in the following estimates as a correction to the derived emission integrals¹³. We believe a reasonable value for the true oxygen abundance $Z_{\text{O,true}}$ is ~ 0.5 , if the X-ray-emitting plasma is ambient disk gas dragged into the halo by the superwind.

Treating the halo region as cylinder of diameter 6.35 kpc and height 6.35 kpc gives a total volume of $V = 5.91 \times 10^{66} \text{ cm}^3$. The electron density in the X-ray emitting plasma in the halo is $n_e = 7.9 \times 10^{-3} \eta_X^{-0.5} \mathcal{R}^{0.5} \text{ cm}^{-3}$. The thermal pressure $P_{\text{TH}}/k = 4.7 \times 10^4 \eta_X^{-0.5} \mathcal{R}^{0.5} \text{ K cm}^{-3}$. The mass of the this gas is $M_X = 4.7 \times 10^7 \eta_X^{0.5} \mathcal{R}^{0.5} M_\odot$, its cooling time and mass cooling rate $t_{\text{cool}} = 770 \eta_X^{0.5} \mathcal{R}^{0.5} \text{ Myr}$ and $\dot{M}_X = 0.06 M_\odot \text{ yr}^{-1}$ (\dot{M}_X depends only on the gas temperature and bolometric luminosity). The mass flow rate $\dot{M}_{\text{flow}} \sim M_X v_x / z = \rho A v_x \sim 7.6 \eta_X^{0.5} \mathcal{R}^{0.5} v_{1000} M_\odot \text{ yr}^{-1}$, where v_{1000} is

¹³While the filling factor dependence of superwind plasma properties is often explicitly noted in published work, the metallicity dependence is generally not shown. The plasma properties of the various superwinds given in the sample Read, Ponman & Strickland (1997) assumed a variety of very low abundances. Strickland, Ponman & Stevens (1997) assumed $Z = 0.05 Z_\odot$ for M82, while Pietsch et al. (2000) assumed Solar abundance in NGC 253’s halo.

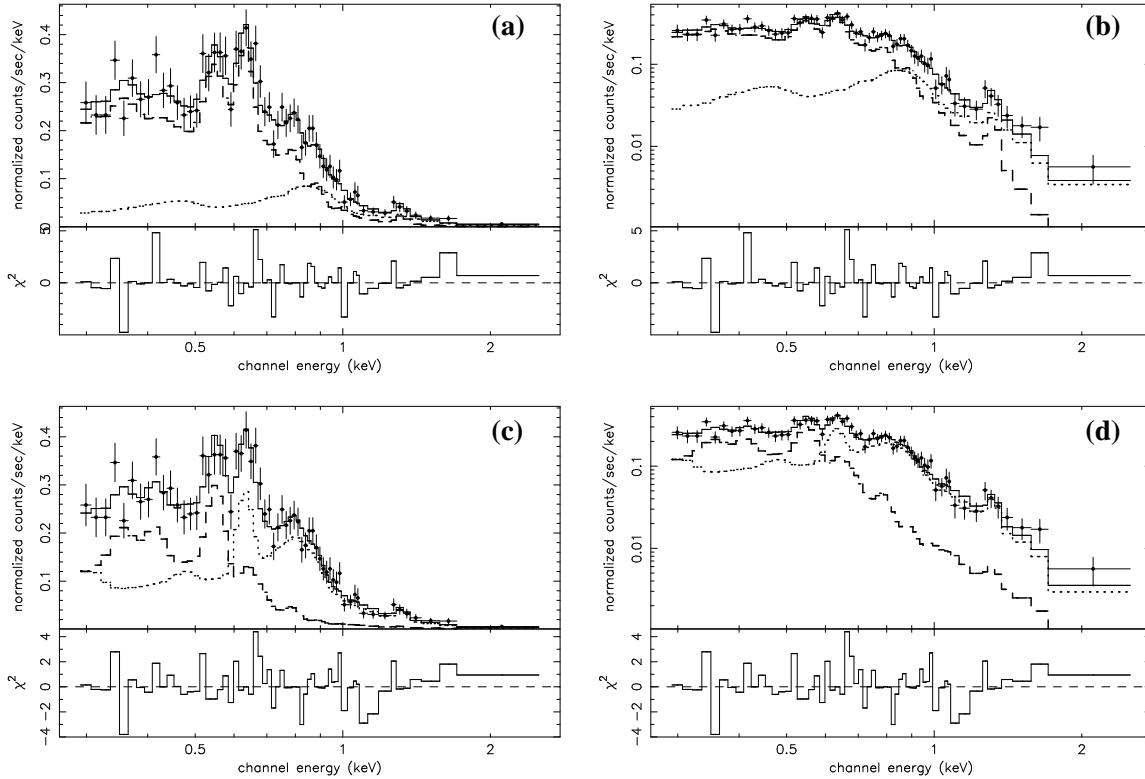


Fig. 8.— The two best multi-phase spectral model fits to the halo spectrum. For details see Tables 3 & 4. The `2Tvapex` model is shown on both linear and log intensity scales in panels (a) & (b). The separate model components are shown as dashed lines. The `2Ivnei` model is shown in linear and log form in panels (c) & (d). The lower panel in each plot shows the contribution to the total χ^2 from each data point.

the outflow velocity of the X-ray emitting plasma in units of 1000 km/s, and we have taken the vertical height of the region z to be 6.35 kpc. The thermal and kinetic energy content of this plasma are $E_{\text{TH}} = 5.9 \times 10^{55} \eta_X^{0.5} \mathcal{R}^{0.5}$ erg and $E_{\text{KE}} = 4.7 \times 10^{56} \eta_X^{0.5} \mathcal{R}^{0.5} v_{1000}^2$ erg.

4.4.2. Upper limits on a high temperature diffuse component

As discussed previously, the detection of counts in the hard X-ray energy band, of marginal significance, is most probably due to systematic problems with background subtraction. If we treat the 2 – 8 keV count rate as a conservative upper limit on the emission from a $kT = 4$ keV plasma component in the superwind, the 2 – 8 keV X-ray flux, luminosity and total emission integral from very hot gas in this region of the superwind are $f_{\text{X,hot}} < 1.4 \times 10^{-13}$ erg s $^{-1}$ cm $^{-2}$, $L_{\text{X,hot}} <$

$$1.1 \times 10^{38} \text{ erg s}^{-1}, \text{ and } EI_{\text{hot}} < 1.4 \times 10^{60} \text{ cm}^{-3}.$$

This is consistent with numerical models of superwinds (Suchkov et al. (1994); Strickland & Stevens (2000)), which predict that although plasma at such temperatures exists within superwinds, it is of such low density that it does not radiate effectively.

5. Point sources and compact clouds in the halo

We detect 30 point-like sources in the S3-chip pointing on the northern halo, that have $S/N \geq 2$ in any of the three broad, soft or hard energy bands (see Table 7). Only three of these sources were detected in previous *ROSAT* PSPC and HRI observations, which were at least 1.5 orders of magnitude less sensitive than our 43 ks *Chandra* observation.

Fig. 2 shows that these sources appear to cluster along the arc of diffuse emission. Could some of them be X-ray-bright clumps or clouds in the wind, as has been suggested on several occasions for some *ROSAT*-detected sources in superwinds (see Read (1994); Strickland, Ponman & Stevens (1997); Vogler & Pietsch (1999))?

5.1. The nature of the point-like sources

We have found optical counterparts for 12 of these sources (Table 8). The high X-ray-to-optical flux ratio of most of these sources are consistent with them being AGN (see Krautter et al. (1999)), although two of the sources (numbers 9 & 16) are without doubt stars given their low X-ray-to-optical flux ratios..

The total number of sources detected in the soft (19) and hard bands (11) with $S/N \geq 2$ is consistent with the numbers expected from deep *Chandra* surveys. The $N \log S$ prescription given in Giaconni et al. (2001) predicts 18 ± 5 and 10 ± 4 sources in the soft and bands over the entire S3 chip, for the flux limit reached in our observation. This suggests that the sources we detect that do not have optical counterparts are nevertheless genuine point-like X-ray sources, primarily AGN, and not false detections of compact clumps in the diffuse X-ray emission.

The spectral properties of these sources (with the exception of the two known stars) are consistent with them being AGN or obscured AGN. Most of these sources are individually too faint to obtain robust hardness ratios from, let alone spectra, but the emission from many sources can be combined to obtain a composite spectrum. As we are interested in whether the faintest sources may be compact features in the diffuse emission we extracted a composite ACIS spectrum from all sources with $2 \leq S/N \leq 3$ that did *not* have any optical counterpart. We refer to these sources as the faint sources, and the composite spectrum as the faint source spectrum. A composite spectrum of the brighter sources ($S/N \geq 3$), and in addition those sources with optical counterparts, but excluding the two known stars, was also extracted (the bright source spectrum). Finally, we also extracted a composite spectrum of the two stars, which we expect to be spectrally softer than the other sources. Source number 20 (a known $z = 1.25$ AGN, see Vogler & Pietsch (1999)),

is sufficiently bright enough to obtain a spectrum from.

An absorbed power law spectral model fit to the bright source composite spectrum gives a best fit photon index of $\Gamma = 1.44^{+0.11}_{-0.12}$ (90% confidence in three interesting parameters), absorbed by a column of $N_{\text{H}} = 1.5^{+1.9}_{-1.3} \times 10^{20} \text{ cm}^{-2}$ ($\chi^2_{\nu} = 1.34$). This is a harder spectrum than a typical AGN ($\Gamma \sim 1.7$), but is consistent with the mean spectrum of the hard X-ray background. The X-ray spectrum of source number 20 is consistent with a typical AGN, the best-fit model giving $\Gamma = 1.66^{+0.30}_{-0.23}$ and $N_{\text{H}} = 4.9^{+3.9}_{-2.4} \times 10^{20} \text{ cm}^{-2}$ ($\chi^2_{\nu} = 1.08$).

Hardness ratios of the bright and faint source spectra are shown in Table 5. The energy bands used (soft: 0.3 – 1.0 keV, hard: 1.0 – 8.0 keV) was chosen to give the largest difference in hardness between the bright sources and the large-scale diffuse emission in the halo. If a significant fraction of the faint sources are indeed dense clumps in the wind, we would expect the hardness of the composite faint source spectrum to be softer than the bright sources, and similar to the hardness ratio of the diffuse emission. This is not the case – the hardness of the faint sources is statistically identical to that of the bright sources, and differs from the hardness of the diffuse emission by at least 6σ . The two X-ray sources identified as stars based on X-ray-to-optical flux ratios are spectrally soft using this hardness ratio test, confirming the identification of the X-ray sources with the optical stars.

Thus it appears that the faint sources seen in the halo of NGC 253 are indeed background AGN and foreground stars unrelated to the superwind itself, based both on number counts and on their spectral properties.

6. H α and X-ray emission in the halo

The relationship between soft X-ray emission and optical H α emission, if present, provides strong clues to the origin of the X-ray-emitting gas in superwinds. It has been long known that there is a strong correlation between X-ray and H α emission in the bright central ~ 1 kpc regions of superwinds (e.g. Watson, Stanger & Griffiths (1984); McCarthy, Heckman & van Bruegel (1987)), robustly confirmed by *Chandra* observa-

TABLE 5
POINT SOURCE HARDNESS RATIOS

Component	$Q_{1-8,0.3-1}$ ^a	Count rate ^b
Bright sources	0.109 ± 0.028	0.0379 ± 0.0010
Source 20 ^c	0.077 ± 0.064	0.0113 ± 0.0006
Faint sources	0.138 ± 0.128	0.0050 ± 0.0006
Stars	-0.580 ± 0.194	0.0037 ± 0.0006
Diffuse halo emission	-0.678 ± 0.031	0.2092 ± 0.0053

^aHardness ratio using the number of counts in the 1.0 – 8.0 keV energy band as the hard band and the counts in 0.3 – 1.0 keV energy band as the soft band. Errors are 68% confidence.

^bTotal ACIS-S3 background-subtracted count rate in the 0.3 – 8.0 keV energy band.

^cSource number 20 is included in the composite bright source spectrum.

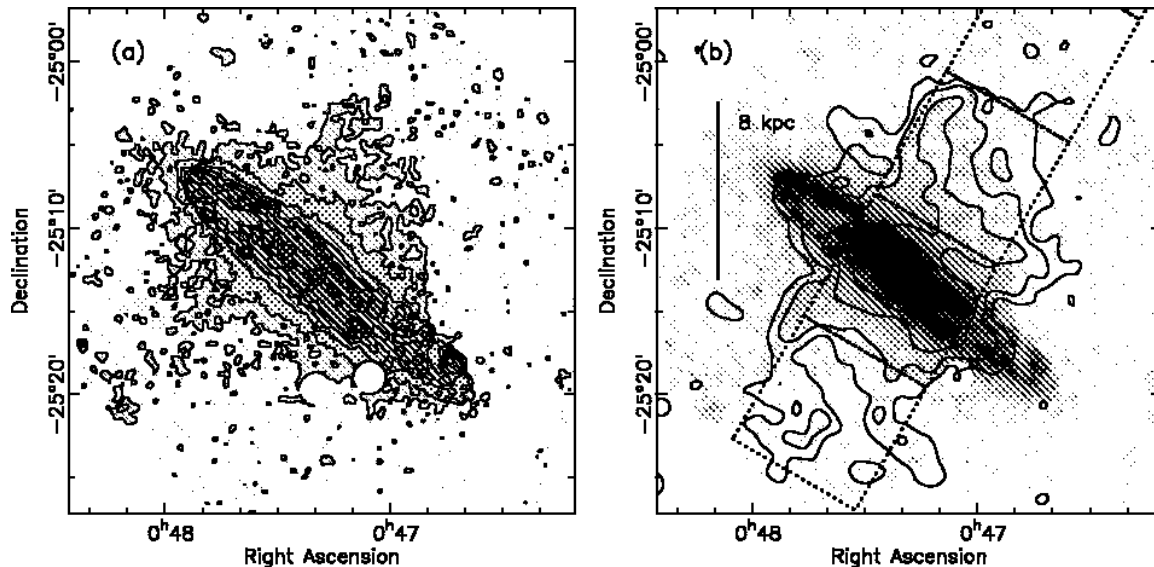


Fig. 9.— (a) Continuum subtracted $H\alpha$ image of NGC 253 showing emission associated with the superwind in the halo of the galaxy. The original image (published in Hoopes, Walterbos & Greenawalt (1996)) has been smoothed with a Gaussian mask of $FWHM = 20''$ in order to bring out the very low surface emission in the halo, and is shown using a logarithmic intensity scale between 10^{-18} and $3.9 \times 10^{-15} \text{ erg s}^{-1} \text{ cm}^{-2} \text{ arcsec}^{-2}$. Contours start at a $H\alpha$ surface brightness of $2 \times 10^{-18} \text{ erg s}^{-1} \text{ cm}^{-2} \text{ arcsec}^{-2}$ and increase in steps of 0.5 dex. Residuals from two saturated star images to the south of the galactic disk have been excised from the image. (b) The $H\alpha$ image overlaid with the contours of soft X-ray emission seen by the *ROSAT* PSPC (Fig. 1b). Dotted lines show the location of the ACIS chips in our *Chandra* observation. The $H\alpha$ image is shown on a logarithmic scale between 10^{-18} and $2 \times 10^{-16} \text{ erg s}^{-1} \text{ cm}^{-2} \text{ arcsec}^{-2}$.

tions in the case of NGC 253 (Strickland et al. 2000).

For several starburst systems with outflows the thermal X-ray and $H\alpha$ emission correlate well on

larger ~ 10 kpc scales (e.g. Arp 220 (Heckman et al. 1996), M82 (Lehnert, Heckman & Weaver 1999)), but no 10 kpc-scale $H\alpha$ emission has been previously noted in the halo of NGC 253, despite

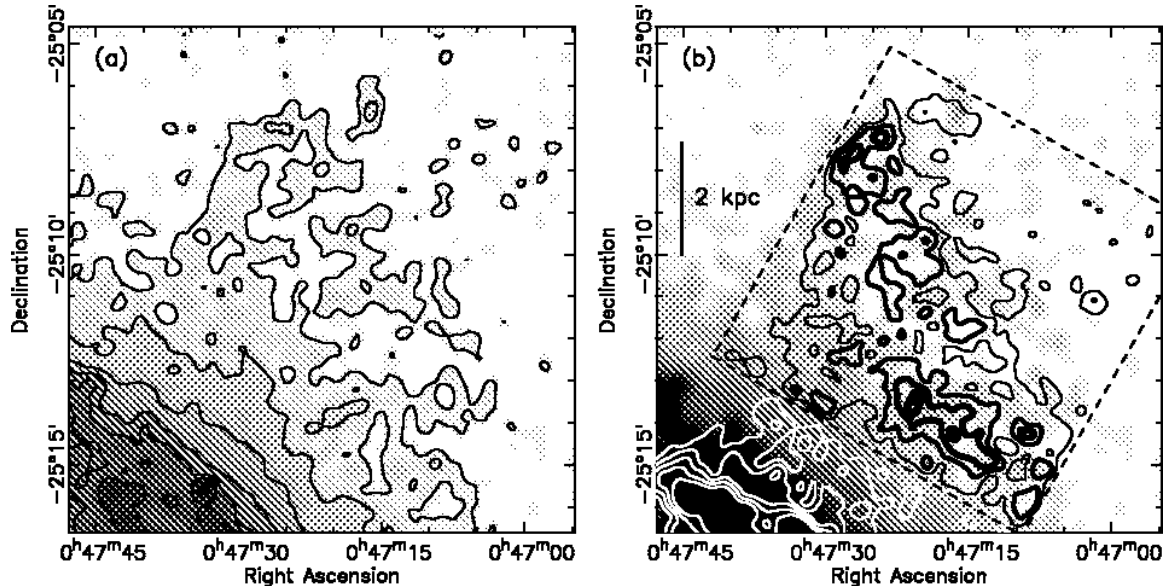


Fig. 10.— (a) As Fig. 9a, except focusing in on the northern halo region to better show the arcs and filaments of $H\alpha$ emission. (b) As Fig. 9b, but focusing in on the northern halo region to better show the relationship between the $H\alpha$ and soft X-ray emission using the $20''$ -smoothed *Chandra* ACIS data, instead of the lower resolution and sensitivity PSPC data. The contours are X-ray S/N = 2, 3, 4 & 5 (see Figs. 3b & 6b), shown with progressively bolder solid lines. The dashed line represents the edges of the S3 chip.

its proximity and status a well-studied archetypal starburst.

Nevertheless, faint $H\alpha$ emission, very similar in morphology to the diffuse X-ray emission, does exist in the halo of NGC 253 (Figs. 9 & 10). To the north of the disk this correlation between X-ray and $H\alpha$ emission is particularly clear. In the northern halo the X-ray emission appears to peak in surface brightness slightly to the west of the peak in the $H\alpha$ emission, although it is difficult to be absolutely confident of this due the small *Chandra* ACIS field of view (Fig. 10), and the heavy smoothing required by the *ROSAT* PSPC data. (Fig. 9). On the southern side of the galaxy, south east of the nucleus, a shorter X-ray arc coincides almost exactly with an $H\alpha$ arc with no discernible spatial offset. Although the morphology of the $H\alpha$ and X-ray emission is very similar on ~ 5 kpc scales, in detail there does not appear to be a exact correlation or anti-correlation on ~ 1 kpc scales.

6.1. $H\alpha$ /X-ray flux ratios

The surface brightness of $H\alpha$ emission in the halo of NGC 253 is ~ 2 orders of magnitude

lower than the typical $H\alpha$ surface brightness in the disk. Our best estimate of the mean surface brightness of the northern halo $H\alpha$ emission is $7.72 \times 10^{-15} \text{ erg s}^{-1} \text{ cm}^{-2} \text{ arcmin}^{-2}$, in the 70.5 arcmin^2 halo region covered by the ACIS S3 chip. The $H\alpha$ luminosity in the halo field is $L_{H\alpha} \sim 4.4 \times 10^{38} \text{ erg s}^{-1}$, comparable to the total luminosity of the soft X-ray emission.

The $H\alpha$ to X-ray flux ratio in this diffuse emission is interesting, as it may provide clues to the physical mechanisms behind both the origin of the X-ray emitting gas and the ionization source of the cool $H\alpha$ emitting gas. Previous work has shown that the soft X-ray and $H\alpha$ fluxes are roughly comparable¹⁴ in both the M82 (Lehnert, Heckman & Weaver 1999) and Arp 220 (Heckman et al. 1996) superwinds.

$H\alpha$ /X-ray flux ratios for the northern halo region and for the clearly-limb-brightened region of

¹⁴Shopbell & Bland-Hawthorn (1998) quote $f_{H\alpha}/f_X \sim 30$ for the brightest $H\alpha$ filaments in M82 based on the *ROSAT* HRI observations. This may be a beam-smearing artefact, given to the much poorer spatial resolution of the HRI compared to their $H\alpha$ observations.

the nuclear southern outflow cone (Strickland et al. 2000) are given in Table 6. Flux ratios are also given for the four northern halo quadrants we defined, (see Fig 2b) which probe a mix of X-ray and H α bright and faint regions.

It is interesting that in all these regions the H α /X-ray flux ratio is generally within a factor 2 of unity. Even in the north western region of the halo, where there is little X-ray and little H α emission, the fluxes are closely matched ($f_{\text{H}\alpha}/f_{\text{X}} = 0.44$).

7. Discussion

7.1. Models for X-ray and H α emission in superwinds

The general correlation between the soft thermal X-ray emission and optical line emission in the halo of NGC 253 (Fig. 9) strongly suggests that these two forms of emission are physically linked, and any meaningful model of superwinds must explain this spatial relationship in addition to the relative fluxes between the two.

In this section we shall assess the physical plausibility of a variety of possible mechanisms for producing both H α and soft X-ray emission in the halo of NGC 253, based on previously published discussions of supernova remnants, wind-blown bubbles, superbubbles and superwinds. A cartoon depiction of some of these possible scenarios is presented in Fig. 11, in the hope of making following discussion clearer to the reader.

7.1.1. Sources of H α emitting gas

There are a variety of possible sources of the cool gas responsible for the H α emission in the halo. An unlikely possibility is that it is cooled superwind SN-ejecta. In-situ halo sources of H α -emitting gas are a radiatively-cooled shell of swept-up halo gas, or radiative shocks driven into pre-existing clouds (e.g. Hester, Raymond & Blair (1994)) within the halo.

The ionization source may be photoionization or shock-heating. Photoionization may be either by UV photons propagating up into the halo from the starburst, or by local sources of energetic photons from the superwind.

7.1.2. Sources of X-ray emitting plasma

Possible sources of X-ray emitting plasma are shocked (Chevalier & Clegg 1985) or mass-loaded (Suchkov et al. (1996); Hartquist, Dyson & Williams (1997)) superwind material, a volume-filling halo medium swept-up and shock-heated by the superwind, or interaction between the wind and clouds in the halo (either pre-existing halo clouds or disk gas dragged into the halo by the wind).

7.1.3. Possible emission models for the halo of NGC 253

Model 1: Cooling radiation from the wind

Could both the X-ray and H α emission come from cooling of the volume-filling wind fluid? The advantages of this model are its simplicity (in that it does not depend on the presence dense gas in the halo), and that it offers the attractive possibility that observations directly probe the enriched gas that drives the wind.

This model requires that the cooling time in the wind is less than, or of order, the age of the outflow. The dynamical age of the gas at the center of the halo region is $t_{\text{dyn}} \sim 6v_{1000}^{-1}$ Myr, where v_{1000} is the mean outflow velocity in units of 1000 km/s. The *minimum* reasonable values of v_{1000} are between 0.3 – 0.6 (see the more detailed discussion of outflow velocity in Model 2 below), which gives dynamic ages of 10 to 20 Myr, similar to estimates of the age of the starburst (Engelbracht et al. 1998). The *radiative* cooling time of the X-ray-emitting gas is $t_{\text{cool}} \sim 770\eta_{\text{X}}^{0.5}\mathcal{R}^{0.5}$ Myr (§ 4.4), significantly longer than the dynamical age of the outflow for any reasonable X-ray filling factor or metal abundance.

Breitschwerdt & Schmutzler (1999) propose a model for soft X-ray emission in 1-dimensional cosmic-ray-driven galactic outflows where the X-ray emitting plasma has a temperature of a few $\times 10^4$ K, due to adiabatic cooling. The X-ray emission arises due to delayed recombination, in which the ions have not had time to come into ionization equilibrium and hence are over-ionized for their kinetic temperature. This neatly bypasses the radiative cooling time problem discussed above.

However, this model can not explain the H α emission seen in superwinds. Although Bre-

TABLE 6
H α /X-RAY FLUX RATIOS AND SURFACE BRIGHTNESSES

Region (1)	Area (2)	$f_{\text{H}\alpha}$ (3)	f_{X} (4)	$\Sigma_{\text{H}\alpha}$ (5)	Σ_{X} (6)	$f_{\text{H}\alpha}/f_{\text{X}}$ (7)
Nuclear cone ^a	0.27	1.81	1.79	186.1	184.2	1.01
Halo (total)	70.51	5.44	5.03	2.1	2.0	1.08
NW halo	17.63	0.27	0.61	0.4	1.0	0.44
NE halo	17.63	1.00	1.26	1.6	2.0	0.79
SW halo	17.63	1.41	1.79	2.2	2.8	0.79
SE halo	17.63	2.76	1.37	4.4	2.2	2.01

NOTE.—Column 1: Spatial region. (2): Geometrical area of region in arcmin². (3): Estimated H α flux in 10^{-13} erg s⁻¹ cm⁻². (4): Estimated soft X-ray flux (0.3–2.0 keV energy band) in 10^{-13} erg s⁻¹ cm⁻², corrected for the area lost due to point sources. This flux estimate has not been corrected for absorption, and is robust across all spectral models. Absorption-corrected fluxes are model dependent, e.g. 20% higher for the 2Ivnei model, and 60% higher for the 2Tvapc model (Table 3). Columns (5) & (6): Mean H α (5) and soft X-ray (6) surface brightnesses in units of 10^{-18} erg s⁻¹ cm⁻² arcsec⁻².

^aThe clearly limb-brightened region of the southern nuclear outflow cone discussed in Strickland et al. (2000).

itschwerdt & Schmutzler (1999) do not consider H α emission, it seems likely that recombination of electrons onto protons at $T \sim$ a few $\times 10^4$ K would lead to spatially correlated H α and soft X-ray emission in this model. However, it is unlikely that the plasma in starburst-driven superwinds expands such that adiabatic cooling leads to low kinetic temperatures. Multi-dimensional hydrodynamical simulations (e.g. Tomisaka & Ikeuchi (1988); Tomisaka & Bregman (1993); Suchkov et al. (1994); Strickland & Stevens (2000)) accurately follow the kinetic temperature of the plasma and all show that internal shocks are extremely common in superwinds, reheating the plasma as kinetic energy is converted into thermal energy in the shocks. This rules out strong adiabatic cooling of the wind giving rise to the H α emission, and probably rules out the specific delayed recombination model in Breitschwerdt & Schmutzler (1999)¹⁵ from applying to starburst-driven superwinds.

Another significant problem with this model, where the emission is distributed smoothly through-

out the wind, is that it does not explain X-shaped morphology of both the X-ray and H α emission.

Hence the model of the X-ray and H α emission as coming from the cooling of the volume-filling wind-fluid can be confidently rejected.

Model 2: Shocked clouds in the halo

A more plausible model is one developed by Lehnert, Heckman & Weaver (1999) to explain an X-ray and H α emitting ridge ~ 12 kpc above M82: a pre-existing neutral cloud (most probably tidal debris associated with the M82/M81 interaction) is over-run by the expanding superwind. A slow shock is driven into the cloud, ionizing it. Photoionization by UV photons escaping from the starburst region may also contribute to the ionization of the cloud. A stand-off bow shock of hot X-ray-emitting superwind gas forms upstream of the cloud. The net result is a close spatial correlation between H α and X-ray emission, both of which are only visible in the vicinity of any halo cloud (see Fig. 11a).

We refer the reader to Lehnert, Heckman & Weaver (1999) for a detailed discussion of this model. We shall only elaborate on some details of the feasibility of the model as applied to the halo

¹⁵We agree whole-heartedly with the more general point Breitschwerdt & Schmutzler (1999) make, which is that collisional ionization equilibrium is unlikely to apply in many regions of galactic outflows.

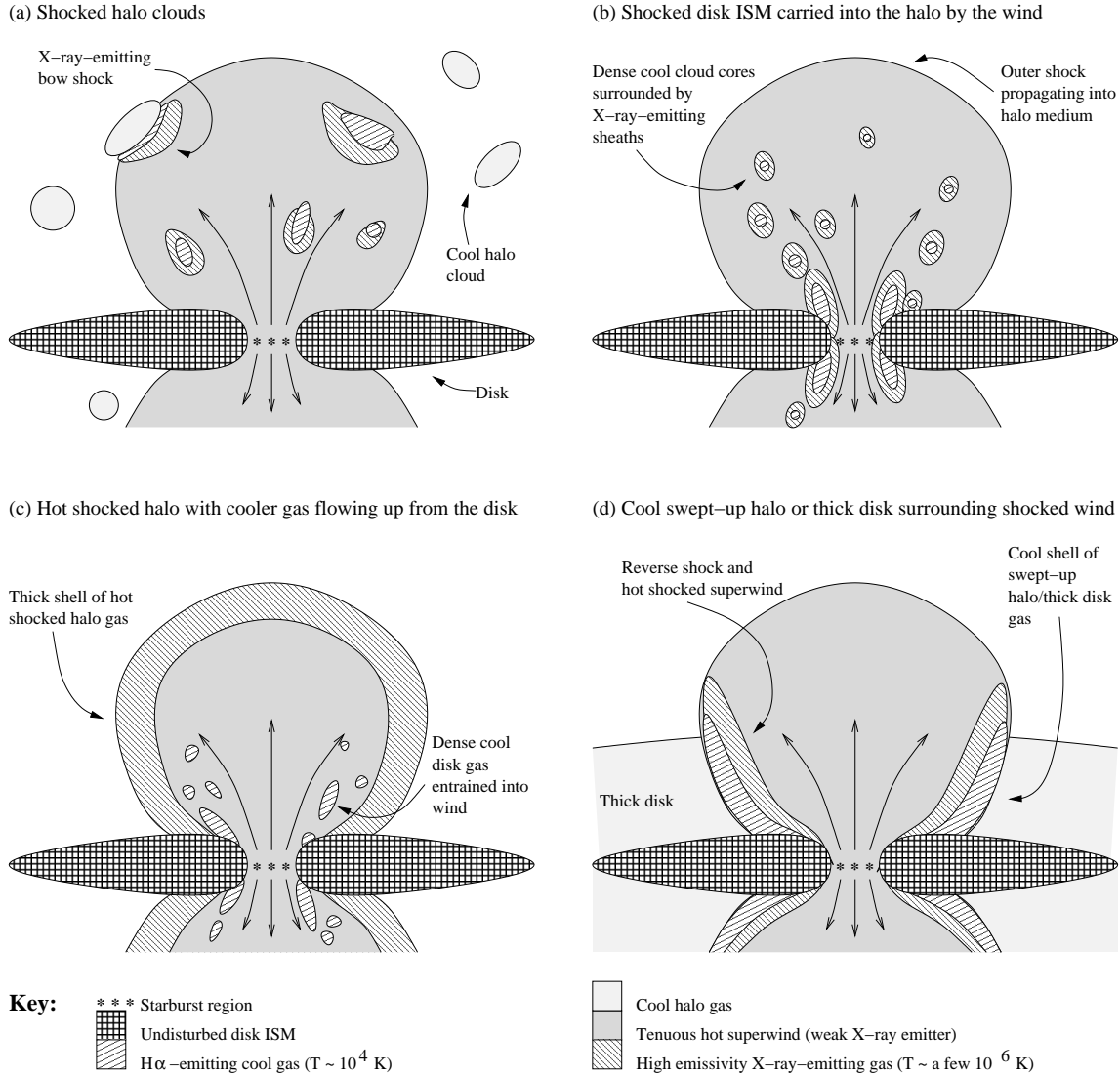


Fig. 11.— A schematic representation of some of the possible situations giving rise to spatially-correlated X-ray and $H\alpha$ emission in the haloes of starburst galaxies, shown as imaginary 2-dimensional slices through the plane described by the major and minor axes of the galaxy. Only one pole of the bipolar outflow is shown in detail. See § 7.1 for details.

of NGC 253 here.

Shock-heating of the wind material in the cloud bow shock to achieve a temperature of $T = 3 \times 10^6$ K requires a shock velocity of $v_s = [(16/3)(kT/\mu)]^{0.5} \approx 470$ km/s. Assuming radiative losses in the starburst region are insignificant, the outflowing SN-ejecta could have velocities as high as 3000 km/s. Spectroscopic measurements of the $H\alpha$ emitting gas in the south-

ern nuclear outflow cone give deprojected outflow velocities of between 340 to 390 km/s (Heckman, Armus & Miley (1990); Schulz & Wegner (1992)) based on an opening angle for the cone of 50 to 65°. Smaller opening angles (e.g. Strickland et al. (2000)) imply the deprojected $H\alpha$ outflow velocity may be ~ 600 km/s. The SN-ejecta which sweeps up and accelerates the $H\alpha$ emitting gas is likely to have higher outflow velocities, so the observed

temperature of the X-ray emitting gas in the halo NGC 253 is easily produced in shocks.

The spectral uniformity of the diffuse X-ray emission is a natural outcome of this model. The temperature of the X-ray emitting gas is simply a function of the shock velocity. A constant X-ray temperature therefore implies the wind velocity is constant within the region considered. The analytical superwind model of Chevalier & Clegg (1985) shows that the wind velocity is approximately constant in the freely expanding wind region, outside the starburst region. Velocities only drop when the wind passes through internal shocks, but rapidly increase again if the gas is given a chance to expand.

The most serious potential constraint upon applications of this model to NGC 253 is the energy requirement *if* the H α emission is energized by shocks. Following the arguments developed by Lehnert, Heckman & Weaver (1999), the power dissipated in a shock is related to the H α luminosity by $L_{\text{shock}} \approx 100L_{H\beta} \approx 33L_{H\alpha}$, based on the calculations of Binette, Dopita & Tuohy (1985). This implies shocks are dissipating the energy in the northern halo of the superwind at a rate $L_{\text{shock}} \sim 1.5 \times 10^{40} \text{ erg s}^{-1}$. Using the *lowest* estimate of the nuclear supernova rate in NGC 253 of $\sim 0.03 \text{ yr}^{-1}$ from Mattila & Meikle (2001) (Ulvestad & Antonucci (1997) provide an upper limit of $< 0.3 \text{ yr}^{-1}$), the mechanical power flowing into the northern halo in the superwind is $\sim 5 \times 10^{41} \eta_{\text{therm}} \text{ erg s}^{-1}$, based on the models of Leitherer & Heckman (1995). Even if we adopt a low value of the supernova energy thermalization efficiency, e.g. $\eta_{\text{therm}} = 10\%$, supernovae can provide more than enough energy to power the H α emission through shocks.

Any contribution to the H α emission from photoionization by the starburst will reduce the implied energy drain on the superwind. Using the arguments of Lehnert, Heckman & Weaver (1999), we can compare the number of ionizing photons required to produce the halo H α emission with the number of emitted in the direction of the northern halo by that starburst, and see if the required “escape fraction” is reasonable. The H α luminosity of the northern halo requires $N_{\text{Ly}\alpha} \sim 4 \times 10^{50} \text{ s}^{-1}$ to maintain. The nuclear starburst produces $N_{\text{Ly}\alpha} > 10^{53} \text{ s}^{-1}$ (Engelbracht et al. 1998), of which a fraction $\Omega/4\pi \sim 0.1 - 0.2$ travel in the direction of the

northern halo. Hence only $\lesssim 4\%$ of these ionizing photons need to escape into the halo to explain the observed H α emission by photoionization alone. This is consistent with current estimates of UV photon escape fractions (e.g. Leitherer et al. (1995); Heckman et al. (2001)) in star-forming galaxies.

Is there any evidence for clouds of neutral gas, or tidal debris, in the halo of NGC 253? The HI studies of Puche, Carignan & van Gorkom (1991) and Koribalski, Whiteoak & Houghton (1995) show no HI structures outside the disk, placing an upper limit on the hydrogen column density in the halo of $> 2.4 \times 10^{20} \text{ cm}^{-2}$ within a $\sim 1'$ beam. The tidal HI features in the halo of M82 have column densities of $\lesssim 1.5 \times 10^{20} \text{ cm}^{-2}$ (Yun, Ho & Lo 1993), so similar features could well be present in the halo of NGC 253 and have escaped detection in the existing HI surveys.

Unless clouds that are over-run by the wind are destroyed on time-scales short compared to the age of the wind, it is difficult to explain the roughly X-shaped morphology of the H α and soft X-ray emission in NGC 253 with this model.

As halo “clouds” or tidal debris are not necessarily symmetrically distributed around the galaxy, this model provides a simple explanation of the often-mentioned asymmetries in superwinds like M82 and NGC 253 (e.g. see discussion in Shopbell & Bland-Hawthorn (1998)), where one pole is typically brighter and more extended than the opposite pole of the outflow. Nevertheless, it remains to be seen how significant wind asymmetries are in larger samples of starburst-driven winds.

Model 3: Shocked disk gas carried into the halo

Motivated by the observations of outflowing H α -emitting gas in the inner several kpc of superwinds, the closely associated soft X-ray emission, and numerical simulations (in particular those of Suchkov et al. (1994)), an alternative model is that the superwind drives cool ambient gas from the disk into the halo, where it is responsible for the observed H α emission. The X-ray emission arises in the vicinity of this cool gas, either in stand-off bow shocks in the superwind material itself, or perhaps in conductive or turbulent mixing interfaces around the cool clumps (see Fig. 11b).

The recent *ISOPHOT* observations of NGC 253

by Radovich, Kahanpää & Lemke (2001), which show X-shaped FIR emission from dust in the same location as the X-ray and H α emission are most easily explained by this model, as the dust is dragged up from the disk along with the H α emitting gas (see also Phillips (1993); Alton, Davies & Bianchi (1999); Heckman et al. (2000)).

Most of the arguments presented in Model 2 can be directly transferred to this model, the only real difference is that the wind brings its own cool gas along with it instead of requiring a pre-existing population of halo clouds. The shock energy dissipation and photoionization arguments about the H α emitting gas remain the same. The temperature of the X-ray emitting gas may again be related to the wind velocity, although it may be more of an emission-weighted mean gas temperature if conductive interfaces or mixing layers dominate in X-ray emissivity over shocked wind.

Simulations show that cool dense gas from the disk of the galaxy is transported into the halo along the walls of the cavity, as Kelvin-Helmholtz instabilities rip off clumps of gas and the wind accelerates them into the halo (see Figs. 3 & 6 in Suchkov et al. (1994), and Fig. 11 of Heckman et al. (2000)). This naturally leads to an X-shaped H α morphology extending out of the disk and into the halo. A thin X-ray-emitting skin covers the clumps of cool gas dragged into the halo. Note that these structures are well within the confines of the wind – they do not mark the outer shock propagating into the halo.

The general H α and X-ray morphology predicted in this model is very similar to that we observe in NGC 253. One minor difference between this model and the observations is that it does not directly predict the systematic offset of the X-ray emission with respect to the H α emission that may exist in the northern halo of NGC 253 (Fig. 10). If the X-ray emission is systematically offset with respect to the interior of the H α emission then Model 3 is in trouble.

Model 4: A hot swept-up shell of halo gas

A useful theoretical approximation is to consider superwinds as superbubbles (Weaver et al. (1977); Mac Low & McCray (1988)) expanding in a low density halo medium, *i.e.* to ignore the presence of the denser ISM in the disk once the superbubble

has blown out into the halo.

A superbubble can be described as a set of concentric regions. Proceeding from the center outwards these are: A central region of mass and energy injection (the starburst region). Out of the starburst region flows a supersonic wind of thermalized SN-ejecta and stellar wind material. The gas properties in these two regions are well-described by the analytical model of Chevalier & Clegg (1985). This region of freely expanding wind is bounded by a shock, commonly referred to as the reverse shock, which separates the free wind from a region of hot shock-heated wind material. A contact discontinuity separates the shocked-wind from a surrounding shell of swept-up shocked ambient gas. An outer shock marks the boundary between the swept-up shell and the surrounding undisturbed ambient medium.

If the cooling time of the shocked ambient gas is small compared to the age of the bubble, the shell cools to $T \lesssim 10^4$ K and forms a thin dense radiative shell, surrounding the non-radiative hot shocked-wind interior to it. This is the physical situation most commonly invoked when considering wind-blown bubbles or superbubbles. Given the high mechanical energy injection rates in starbursts, along with the assumption that the gas density in the halo is low, it is quite possible that the swept-up shell may still be hot and an appreciable source of soft X-ray emission (Fig. 11c). We will discuss the case of a cool shell in Model 5 below.

Is this model consistent with the observational data? For a bubble driven into a medium of constant density ρ_0 , by a wind with a mechanical power $\dot{E}_w = L_w$, the radius of the bubble as a function of time t is $R_s = 0.76 L_w^{1/5} \rho_0^{-1/5} t^{3/5}$ (Castor, McCray & Weaver 1975). The age of the bubble, its radius and the velocity of the outer shock are related by $t = 0.6 R_s / v_s$. If we assume that the velocity of the outer shock in the halo of NGC 253 is $v_s = 470$ km/s (which gives a post-shock temperature of 3×10^6 K), and the radius $R_s \sim 10$ kpc, then the dynamical age is $t_{\text{dyn}} = 12.5$ Myr. Adopting the lower estimate of the SN rate discussed in Model 2, and assuming the thermalization efficiency is unity, $L_w \sim 10^{42}$ erg s $^{-1}$. Solving for ρ_0 we obtain $\rho_0 = 5.5 \times 10^{-28}$ g cm $^{-3}$, implying a total initial halo mass of $M \sim 4\pi R_s^3 \rho_0 \sim 3.4 \times 10^7 M_\odot$ of gas within a radius R_s has been

swept-up and shock-heated.

The cooling time of this gas is longer than the dynamical age of the bubble, as required to maintain a hot shell. For isobaric cooling at Solar abundance, the cooling time t_c from an initial temperature of 3×10^6 K down to 10^4 K is $t_c = 2.8 \times 10^5 n_e^{-1}$ years, based on numerically integrating the non-ionization equilibrium cooling curves of Sutherland & Dopita (1993)¹⁶. Assuming the outer shock is strong, the electron number density in the shocked shell of halo gas is $n_e \sim 2\rho_0/\mu \sim 1.1 \times 10^{-3} \text{ cm}^{-3}$, where $\mu = 10^{-24}$ g. The cooling time of the halo in this model is $t_c \sim 2.5 \times 10^8$ years, an order of magnitude greater than the dynamical age of the bubble.

The implied X-ray emission integral $EI = n_e n_H V \approx n_e^2 \times M/2\mu n_e \sim 3.8 \times 10^{61} \text{ cm}^{-3}$, agreeably close to the order-of-magnitude observation estimates of the emission integral presented in § 4.4.

Thick, X-ray-emitting shells of swept-up shocked halo gas are found in the numerical simulations of both Suchkov et al. (1994) and Strickland & Stevens (2000), where the mean expansion velocities of the wind are ~ 1000 km/s in the halo and densities are too low to allow significant cooling. The 2-D X-ray emissivity maps in Suchkov et al. (1994) demonstrate that the largest volume of moderately high X-ray emissivity gas in 0.1 – 2.2 keV energy band is this shell of shocked halo gas, and it contributes approximately half of the total soft X-ray luminosity.

This does not prove that the X-ray emitting gas in the halo of NGC 253 is a hot shell of swept-up shell of halo gas, merely that this model is consistent with the X-ray data.

The most significant and troubling problem with this model is where does the spatial correlation with the H α emission come from? The most plausible origin for X-shaped distributions of cool gas in the haloes of starburst galaxies is that it is dragged up by the wind, from along the walls of the superwind cavity within the disk, *i.e.* as presented in Model 3. The cartoon of Model 4 presented in Fig. 11c, which is based on numeri-

cal simulations, would imply that the H α emission would lie within the X-ray emission, which does not seem to be the case.

If this model (or Model 3, which also predicts hot gas beyond the region of dense H α emitting gas) is correct, the *XMM-Newton* observations of NGC 253 might be able to detect the faint presence of the wind beyond the H α emitting regions, given the larger field of view of the EPIC instruments compared to ACIS. For other more distant edge-on starbursts like NGC 3628 and NGC 3079 the ACIS field of view is large enough to test the idea that X-ray emission may extend beyond any H α emission.

Model 5: Swept-up thick-disk and shocked wind

If the swept-up shell does cool, the result is a H α -emitting shell surrounding a hot bubble of shocked SN-ejecta. In the Weaver et al. (1977) wind-blown bubble model, X-ray emission from this region of hot, shocked, gas is concentrated near the cool shell, because thermal conduction partially evaporates the shell into the hot bubble, locally increasing the X-ray emissivity.

This naturally produces limb-brightened H α emission with soft X-ray emission concentrated slightly interior to the H α emission. Applied to superwinds expanding into a galactic halo, the observed morphology would approximate a figure-eight centred on the starburst nucleus if the gas density in the halo is uniform, or an open-ended X is the halo gas density decreases with increasing height above the plane of the galaxy (as depicted in Fig.11d).

Given the lack of an obvious cap to the superwind in NGC 253, a plausible model is that this halo material represents some form of thick disk component with a scale-height of several kpc, possibly lifted above the thin disk by the star-formation activity within the disk, as seen in the numerical simulations of Rosen & Bregman (1995). Narrow-band optical imaging strongly suggests that the presence of extended H α emitting gas in the halos of non-starburst galaxies correlates with the strength of star-formation activity in the disk (see for example Rand (1996); Wang, Heckman & Lehnert (1997); Hoopes, Walterbos & Rand (1999)). If so, then the expansion of the superwind into this material can be used as a probe of the distribution of gas in the halos of disk

¹⁶A useful approximation based on these calculations is that for isobaric cooling at Solar abundance $t_c n_e \approx 4000 \text{ yr cm}^{-3}$ for $4.4 < \log T < 5.4$, and $t_c n_e \approx 4000 (T/10^{5.4})^{1.7} \text{ yr cm}^{-3}$ for $5.4 \leq \log T < 8.0$.

galaxies (Sofue & Vogler 2001).

In order for the shocked halo to cool, the shock velocity has to be relatively low and the post-shock density reasonably high – effectively the more gas there is in the halo the more likely it will be for the swept-up shocked halo to cool rapidly. For convenience we assume a shock velocity of 210 km/s, as the resulting post-shock temperature is 6×10^5 K. This is the critical temperature adopted by Castor, McCray & Weaver (1975) below which they assumed the shell cools rapidly.

Following the same method as presented in Model 4, the dynamical age of the bubble is 27.9 Myr, and for $L_w = 10^{42}$ erg s⁻¹ the required initial density and gas mass are $\rho_0 = 6.2 \times 10^{-27}$ g cm⁻³ and $M = 3.8 \times 10^8 M_\odot$.

The initial-post shock electron number density, prior to cooling, is $n_e = 1.24 \times 10^{-2}$ cm⁻³. The isobaric cooling time at $T = 6 \times 10^5$ K is $t_c \approx 1.8 \times 10^4 n_e^{-1}$, *i.e.* $\approx 1.5 \times 10^6$ years. As this is $\sim 1/20$ th of the dynamical age of the wind, it is clear that the shocked halo can cool down to $T \sim 10^4$ K, and be a source of the observed H α emission. Note that the total mass of swept-up gas in the example above is larger than the observed mass of H α emitting gas in the northern halo, which we estimate to be $M_{\text{H}\alpha} \approx 4 \times 10^6 \eta_{\text{H}\alpha} M_\odot$ (where $\eta_{\text{H}\alpha}$ is the fraction of the total halo volume currently occupied by the H α emitting gas). In principle there is nothing preventing the dense gas in the shell cooling below 10^4 K and hence not contributing to the observed H α flux, so the requirement that there is a few times $10^8 M_\odot$ of gas in the halo is not a significant problem for this model. The average hydrogen column density through the halo assuming a total mass of $3.8 \times 10^8 M_\odot$ is crudely $N_{\text{H}} \sim M/4\pi R_s^2 \sim 1.3 \times 10^{20}$ cm⁻², below the current observation limits for HI studies of NGC 253.

An interesting prediction of this model is a high OVI flux from the cooling region behind the outer shock (provided $v_s \gtrsim 150$ km/s). For the example parameters discussed above, we predict a OVI column density through the shock of 5×10^{14} cm⁻², and a total emitted luminosity in the OVI $\lambda\lambda$ 1032, 1038 doublet of $\sim 7 \times 10^{40}$ erg s⁻¹. A large fraction of the energy radiated by the cooling shocked halo gas is carried by OVI emission.

This model has the appealing conceptual advantage over the previous models in that it eas-

ily explains the morphology of the H α and X-ray emitting gas, and leads to the interesting possibility that we might probe be able to observationally probe some function of the halo gas density and superwind ram pressure at ~ 10 kpc distances above the plane of the galaxy. In contrast the H α /Xray morphology in Model 3 does not tell us the location of the outer shock of the wind, instead depending on the complex physics of gas entrainment from the disk by the wind. Nevertheless, the viability of this model depends crucially on the ability of the shocked halo material to cool, and this model predicts larger gas masses in the halo than implied by the observed H α flux alone. More sensitive HI observations of NGC 253 would be of great use for constraining both this model and Model 2.

7.2. Magnetic fields in the halo

We have ignored the role of magnetic fields in the previous discussion. This appears justified based on a comparison between the energy density in hot gas with that in magnetic fields and cosmic rays. The minimum energy B-field strength in the halo is $\sim 2 \mu\text{G}$ (Carilli et al. (1992); Beck et al. (1994)). The ratio of the energy density in this field to the thermal pressure of the X-ray emitting plasma is $\sim 0.025 \eta_{\text{X}}^{0.5} \mathcal{R}^{-0.5}$, which suggests magnetic fields are dynamically unimportant.

The orientation of the magnetic field in the lower halo of NGC 253 ($z \sim 3$ kpc, *i.e.* roughly at the base of the northern ridge) is parallel to the disk (Beck et al. 1994), in contrast to the radial magnetic field structure in the halos of M82 (Reuter et al. 1994) and NGC 4631 (Golla & Hummel 1994). This reasonably lead Beck et al. (1994) to suggest that the magnetic field structure in halo of NGC 253 suppressed the superwind from flowing further into the halo. This now seems unlikely, given the relatively weak field estimated above. Further evidence against the idea of wind suppression, and supporting the idea that magnetic fields are dynamically weak, is the clear presence of both X-ray and H α emission further out in the halo beyond the region of parallel B-fields..

7.3. Implications for understanding the superwind phenomenon

It is worthwhile to take a step back from the minutiae of the different models presented in the previous sections to consider the broader implications of these observations for understanding starburst-driven outflows.

Strong similarities between H α and X-ray morphology over a range of spatial scales, from 100's of pc to ~ 10 kpc, have been found in both M82's starburst-driven superwind (see in particular Watson, Stanger & Griffiths (1984); Dahlem, Weaver & Heckman (1998); Shopbell & Bland-Hawthorn (1998); Devine & Bally (1999) & Lehnert, Heckman & Weaver (1999)) and the ultra-luminous IR galaxy Arp 220 (Heckman et al. (1996); Jonathan McDowell, private communication). In the other nearby edge-on starbursts with superwinds, such as NGC 253, NGC 3079 & NGC 3628 such global (10 kpc-scale) H α /X-ray relationships had not previously been found (Dahlem et al. (1996); Read, Ponman & Strickland (1997); DWH98; Pietsch, Trinchieri & Vogler (1998); Pietsch et al. (2000)). The detection of H α emission similar in flux the X-ray emission in the halo of NGC 253 (a far more typical starburst galaxy than M82 or Arp 220) suggests that *all* superwinds may have large-scale H α halos.

Physically meaningful models of superwinds *must* be able to simultaneously explain the presence, relative spatial distribution and relative fluxes of X-ray and H α emission in the haloes of starburst galaxies. Models that satisfy X-ray constraints only, for example delayed recombination (Breitschwerdt & Schmutzler 1999) or the Bipolar Hypershell model of Sofue & Vogler (2001), fail to predict the observed H α emission.

Our ability to infer the properties of superwinds depends on knowing the physical origin of the emission. As the previous section has shown, there are a variety of possible models that can explain spatially correlated X-ray and H α emission. Depending on which model is chosen different inferences about superwind properties can be drawn. For example, in Model 2 the X-ray-emitting plasma is shocked superwind and its temperature a measure of the wind velocity, while in Model 3 the X-ray emission may come from conductive interfaces or turbulent mixing layers

around clouds, and its temperature may have little to do with the wind velocity. Instead the X-ray and H α emission tell us about mass entrainment of disk ISM by the wind and its transport into the halo. In Model 5 the presence of H α emission immediately places limits on the velocity of the outer shock and the properties of pre-existing halo gas, whereas it is the X-ray data that encodes this information in Model 4. In models 4 and 5 the X-ray and H α emission mark the outer boundary of the wind, in Model 3 the wind can extend far beyond the H α and X-ray bright region. All of the above models have been selected in an attempt to satisfy the (admittedly loose) observational constraints, yet they each carry very different implications for our understanding of winds.

If the H α emission is due to cool gas transported out of the disk by the action of the superwind (Models 3 & 4), it suggests that it is not only the hottest gas phases that escape the gravitational potential of the host galaxy.

Superwinds are without-doubt extremely complex, and it is quite possible that two or more of the different models presented above may apply within a single galaxy. The best interpretation for the X-ray/H α ridge 12 kpc north of M82 is the halo cloud model of Lehnert, Heckman & Weaver (1999), but Models 3, 4 or 5 may best describe the emission closer to M82's disk.

The most fundamental discriminant between these models are the details of the exact spatial location of the H α emission with respect to the X-ray emission. More quantitative properties are unfortunately biased by the long standing problems of observationally unknown volume filling factors and the systematic problems associated with the X-ray-determined abundance determinations. In NGC 253 the limited field of view of the ACIS instrument has somewhat restricted our ability to apply these discriminants, but for slightly more distant starbursts, e.g. NGC 3628 and NGC 3079, *Chandra* will be the ideal instrument.

8. Summary

We have presented a detailed case study of the diffuse X-ray emission from a starburst-driven superwind in the closest typical starburst galaxy, NGC 253. The main results of this study can be summarized as:

1. The diffuse X-ray emission appears to outline an X-shaped structure centered on the starburst nucleus, although the north western and south western arms of the X are relatively indistinct. The ridge-or-arc-like feature in the northern halo forms part of the bright north eastern limb of the X.
2. We have uncovered a similar, previously unreported, X-shaped-feature in $H\alpha$ images of NGC 253, very similar to the soft X-ray emission and extending ~ 8 kpc above the plane of the galaxy. Very extended $H\alpha$ emission is likely to be a general feature of all superwinds.
3. Based on our *Chandra* data, there is no statistically significant variation in the spectral properties of the diffuse X-ray emission in the northern halo, over scales of several 100 pc to several kpc.
4. Spectral features due to highly ionized O, Fe, Mg and possibly other elements robustly demonstrate a thermal origin for at least some fraction of the soft X-ray emission in the halo of NGC 253, although the unphysically low abundances derived from spectral fitting indicate that we do not fully understand the X-ray spectra of starbursts. One possibility is a non-thermal X-ray contribution, perhaps synchrotron emission associated with the cosmic rays and magnetic fields dragged into the halo by the superwind.
5. The marginal detection of diffuse emission in the 2 – 8 keV band is most likely due to background subtraction problems, and not due to a very hot superwind component. We can only place upper limits on the presence of any spectrally-hard diffuse component, with $L_{X,\text{hard}} < 10^{38} \text{ erg s}^{-1}$ assuming a plasma temperature of $kT = 4$ keV.
6. Soft X-ray and $H\alpha$ fluxes are very similar in the northern halo, consistent with the X-ray to $H\alpha$ flux ratios found in other starbursts, and to those in NGC 253's nuclear outflow cone.
7. The total X-ray and $H\alpha$ luminosities of the northern halo region are $L_X \sim 4.9 \times 10^{38} \text{ erg s}^{-1}$ (0.3 – 2.5 keV) and $L_{H\alpha} \sim 4.4 \times 10^{38} \text{ erg s}^{-1}$. Other plasma properties are more uncertain, given the unknown metal abundance and filling factor of the X-ray-emitting plasma. Photoionization by UV photons escaping the starburst can explain the ionization of the $H\alpha$ emitting gas. Alternatively, if the $H\alpha$ emission were powered by shocks alone this implies a power dissipation in the northern halo shocks of order $\sim 1.5 \times 10^{40} \text{ erg s}^{-1}$. This is value is still well below the minimum energy injection rate by the starburst, so we conclude radiative energy losses in superwinds are minimal.
8. The spatial distribution of the $H\alpha$ and *Chandra* X-ray emission in the halo is similar on several kpc scales, but at smaller scales there is no clear correlation or anti-correlation. In the northern halo the X-ray emission appears offset towards the interior of the superwind from the $H\alpha$. In the southern halo the X-ray and $H\alpha$ emission do not appear to be offset from each other, although this inference is based on the lower spatial resolution *ROSAT* PSPC data. Successful models of superwinds must be able to simultaneously explain both the X-ray and $H\alpha$ emission.
9. Sofue & Vogler (2001) have pointed out that the location of the outer boundary of the X-ray emission in superwinds may provide a convenient method of probing the relatively unknown density distribution in the halo of galaxies. This relies upon the observed X-ray emission marking the edge of the wind, which we emphasize is not necessarily the case. Explaining the $H\alpha$ emission we have found, which appears to envelope the X-ray emission in the halo NGC 253, in a Sofue & Vogler-like model appears difficult. Models based on the Weaver et al. (1977) wind-blown model show that the shell of swept-up halo gas may be the origin of the $H\alpha$ emission in the halo, if there was a sufficient density of gas in the halo to allow it to cool in less than a dynamical time.
10. We present and discuss a variety of plausible models that aim to explain the correlated X-ray and $H\alpha$ emission. There are a variety

of possible physical origins of the X-ray and H α emission, each which have different implications for our understanding of the properties of superwinds and the halo gas they expand into. We find that the relative spatial location of the H α emission with respect to the X-ray emission is the most robust discriminant between the various models.

In the longer term a combination of this detailed study of the halo of the nearest classic starburst NGC 253, combined with *Chandra* and H α observations of a larger sample of superwinds, will determine which of the possible modes of coupled X-ray and H α emission is the most common in superwinds.

It is a pleasure to thank the anonymous referee for a considered, helpful, and prompt report. We would like to thank Jonathan McDowell, Tahir Yaqoob, Ed Colbert, Nancy Levenson & Nichole King for helpful advice and suggestions. The team that built and operates *Chandra* also deserves recognition, for their hard work, and for making such an excellent telescope. DKS is supported by NASA through *Chandra* Postdoctoral Fellowship Award Number PF0-10012, issued by the *Chandra* X-ray Observatory Center, which is operated by the Smithsonian Astrophysical Observatory for and on behalf of NASA under contract NAS8-39073. This research has made use of data obtained through the High Energy Astrophysics Science Archive Research Center Online Service, provided by the NASA/Goddard Space Flight Center. This work was supported in part by NASA through grants LTSA NAG56400 and GO0-1008X.

A. Source searching methods

We used two different techniques to search for X-ray point sources in the halo of NGC 253: the wavelet-based WAVDETECT and the simpler sliding box method CELLDTECT. Both of these are routines provided as part of CIAO. Each of these methods has its own distinct set of strengths and weaknesses. Comparing sources detected by both methods to the aperture method described below revealed biases in both the wavelet and sliding box source detection algorithms. WAVDETECT provided apparently accurate estimates of the total number of source counts in each source, but the uncertainties on the total source counts it quotes were sub-Poissonian and hence overestimated the significance of the faintest sources. CELLDTECT, on the other hand, gave realistic uncertainties for a given number of source counts, but systematically underestimated the total counts in each source and hence underestimated the source significance.

Both of these methods detected large numbers of apparently faint point sources that appear to be spurious mis-identifications of local enhancements in the diffuse emission as point sources, given that each method detected a different set of sources at low S/N , that these sources appeared to follow the distribution of the diffuse emission, and that these detections were in the soft 0.3–2.0 keV X-ray band.

Source searching the halo region of NGC 253 is relatively difficult, given the presence of both moderate and low surface brightness diffuse emission, irregularly distributed over the chip. The biases in the standard source detection algorithms may well be related to the unavoidable difficulty of robustly detecting point sources under such conditions. We therefore used both WAVDETECT and CELLDTECT to identify point *source candidates*. To find the true count rate, count rate uncertainties and source significance of any candidate, we used a method inspired by the source searching procedures described in Giacconi et al. (2001).

A list of candidate sources was created by source searching images of the entire S3 chip created in three energy bands (soft X-rays: 0.3–2.0 keV, hard X-rays: 2.0–8.0 keV and broad band: 0.3–8.0 keV energy band) with both wavelet and sliding box methods. All six resulting lists of candidate sources were merged, accepting as a potential source any detection with a signal-to-noise ratio (S/N) greater than 1.5 using either method, but removing any duplicate detections.

We then calculated the source count rate and uncertainty by measuring the counts in a circular source region, and in an encompassing local background region. To estimate the true source counts and uncertainty from these measurements we used the method detailed in § 5 of the CIAO Detect Guide (Dobrzycki et al. 1999), which uses Gerhel’s (1986) formula for the uncertainty ($\sigma_N \approx 1 + \sqrt{(0.75 + N)}$) as a good approximation to the Poissonian nature of the errors. Note that this is the same theory as is used in the CELLDTECT source searching algorithm. The main differences between our method and CELLDTECT are: (a) the source and background regions we use are larger than those used by CELLDTECT (see below), and (b) we ensure that no background or source region encloses counts from any other nearby point source (a problem that will have affected CELLDTECT in several instances for this observation).

We empirically derived the variation in the size of the ACIS PSF as a function of off-axis angle in the S3 chip using 12 bright point sources, using this observation and our separate S3 chip observation of the disk of NGC 253, by fitting two dimensional Gaussian models to each point source. This allows us to scale the size of the source extraction region used to calculate the source counts rates realistically with off-axis angle. We used a source extraction radius equal to the maximum of either $3''$ or the 4 sigma radius of the empirical PSF (the 4σ radius is $1''.35$ on-axis, and $9''.4$ at an off-axis angle of $6'$). We used a circular background region of radius $15''$ in all cases, which always fully enclosed the source region, but in many cases was offset from the center of the source region to avoid including counts from other nearby source candidates. These source and background regions are significantly larger than those used in CELLDTECT (for example, the on-axis source region is a square region of only 9 pixels, whereas our smallest source region comprises ~ 110 pixels). As significant numbers of counts can be seen to fall outside the standard 9 pixel CELLDTECT boxes in the brighter sources, we believe that this leads to CELLDTECT underestimating the total source count rates. Experimentation showed that as the size of the source and background regions are increased (starting from the same size as used by CELLDTECT), the estimated source count rates increased. Once the size of the source and background regions approached the values we adopted, the estimated source counts and errors

had converged.

Of an initial list of 86 candidate sources, this method arrived at a total of 30 unique sources of $S/N \gtrsim 2.0$, of which 13 sources had $S/N \gtrsim 3.0$. Although a S/N ratio of 2.0 is low, many of these low significance sources are likely to be genuine, as they have clear optical counterparts in deep CCD images (see § 2.2.1). The positions, count rates, fluxes and any optical identifications of these sources are given in Table 7. The brightest of the sources, e.g. source number 20, may be of use in the future for UV and X-ray absorption line studies of superwinds (e.g. Norman et al. (1996)).

B. The significance of diffuse emission features

For the purposes of completeness we describe the method used to calculate the relationship between X-ray surface brightness and the significance of that feature above the background.

After the removal of point sources, the remaining X-ray emission consists of a diffuse component (of surface brightness Σ_D in units of count s^{-1} arcsec $^{-2}$) and a background component (the soft and hard X-ray backgrounds, with surface brightness Σ_{BG}). In an observation of length t_1 the total number of counts N_T , detected within an aperture of area A square arcseconds, is the sum of the diffuse and background components $N_T = N_D + N_{BG}$. The signal-to-noise ratio R of a feature in a background-subtracted image is

$$R = \frac{N_D}{\sqrt{(\sigma_D^2 + \sigma_{BG}^2 + \sigma'_{BG}{}^2)}} = \frac{\Sigma_D t_1 A}{\sqrt{(\Sigma_D t_1 A + \Sigma_{BG} t_1 A [1 + t_1/t_2])}}, \quad (\text{B1})$$

where $\sigma_D^2 + \sigma_{BG}^2 = \sigma_T^2$ is the variance in the total number of counts detected within the aperture, and $\sigma'_{BG}{}^2$ is the variance associated with background image used in background subtraction, correctly scaled to the exposure time of the observation. We use the composite background fields provided by the CXC to estimate Σ_{BG} , where the length of the background field observation $t_2 = 114866$ s for the S3 chip and 201452 s for the S2 chip.

Solving for Σ_D we find

$$\Sigma_D = \frac{R^2 A \pm (A^2 R^4 + 4 \Sigma_{BG} R^2 A^3 t_1 [1 + t_1/t_2])^{1/2}}{2 A^2 t_1}. \quad (\text{B2})$$

From the composite background fields the mean background surface brightness in the S3 chip is $\Sigma_{BG} = 8.415 \times 10^{-7}$ counts s^{-1} arcsec $^{-2}$ in the soft 0.3 – 2.0 keV band, and $\Sigma_{BG} = 1.121 \times 10^{-6}$ counts s^{-1} arcsec $^{-2}$ in the hard 2.0 – 8.0 keV band. For the S2 chip the equivalent background surface brightnesses are 3.814×10^{-7} and 5.892×10^{-7} counts s^{-1} arcsec $^{-2}$. The X-ray surface brightness required to obtain a given signal-to-noise ratio in an aperture of a given diameter for the S3 chip is given in Table 9.

C. Hardness maps

C.1. Hardness ratios

For counts H and S , extracted from two independent energy bands where H represent the counts in the higher energy (hard) band and S the counts in the lower energy band, the hardness ratio $Q = (H - S)/(H + S)$. If both H and S are ≥ 0 , then this hardness ratio has the nice property that $-1 \leq Q \leq 1$.

The uncertainty in any single measurement of the number of counts N is $\sigma_N \approx 1 + \sqrt{0.75 + N}$, where we have used the conservative approximation to Poisson errors from Gehrels (1986). The uncertainty in the hardness ratio σ_Q is

$$\sigma_Q \approx \frac{\sigma_{H+S}}{(H + S)} (1 + Q^2)^{1/2}. \quad (\text{C1})$$

TABLE 7
X-RAY POINT SOURCES IN THE NORTHERN HALO

ID	Official name (CXOU number)	α (J2000) (h m s)	δ (J2000) ($^{\circ}$ ' ")	Background-subtracted counts ^a			f_x ^b	Previous ^c detections
				(broad band)	(soft band)	(hard band)		
1	J004659.1-250814	00 46 59.06	-25 08 14.5	16.0 \pm 8.8	14.8 \pm 7.3	1.6 \pm 5.9	0.24 \pm 0.13	...
2	J004659.7-251209	00 46 59.68	-25 12 08.6	17.9 \pm 6.8	12.0 \pm 5.4	5.9 \pm 4.8	0.27 \pm 0.10	...
3	J004701.1-250843	00 47 01.13	-25 08 42.8	7.2 \pm 9.0	-7.2 \pm 6.6	14.4 \pm 7.0	0.11 \pm 0.14	...
4	J004701.9-251108	00 47 01.89	-25 11 08.1	13.8 \pm 7.2	13.3 \pm 6.5	0.5 \pm 4.1	0.21 \pm 0.11	...
5	J004703.0-251028	00 47 03.03	-25 10 27.9	13.8 \pm 6.8	-0.1 \pm 4.3	13.8 \pm 5.9	0.21 \pm 0.10	...
6	J004708.6-250714	00 47 08.60	-25 07 14.0	48.2 \pm 11.7	36.0 \pm 8.9	12.2 \pm 8.4	0.73 \pm 0.18	...
7	J004709.6-251404	00 47 09.61	-25 14 04.2	410.0 \pm 21.4	383.3 \pm 20.7	26.7 \pm 6.4	6.21 \pm 0.32	R5, DWH3, VP13
8	J004709.8-251513	00 47 09.85	-25 15 13.2	15.0 \pm 5.6	9.6 \pm 4.6	5.4 \pm 4.0	0.23 \pm 0.08	...
9	J004711.2-251333	00 47 11.18	-25 13 33.4	11.5 \pm 5.0	11.8 \pm 4.9	0.2 \pm 2.3	0.17 \pm 0.08	...
10	J004712.8-251452	00 47 12.80	-25 14 51.6	9.8 \pm 4.9	8.7 \pm 4.6	1.1 \pm 2.7	0.15 \pm 0.07	...
11	J004713.1-251240	00 47 13.14	-25 12 39.7	9.3 \pm 4.6	4.4 \pm 3.6	4.9 \pm 3.6	0.14 \pm 0.07	...
12	J004716.1-250713	00 47 16.14	-25 07 13.0	35.4 \pm 10.1	8.1 \pm 7.1	27.3 \pm 7.9	0.54 \pm 0.15	...
13	J004716.2-251306	00 47 16.19	-25 13 06.3	11.8 \pm 5.0	8.1 \pm 4.3	3.7 \pm 3.4	0.18 \pm 0.08	...
14	J004717.6-250603	00 47 17.65	-25 06 02.9	21.8 \pm 9.8	18.6 \pm 8.0	3.2 \pm 6.5	0.33 \pm 0.15	...
15	J004718.3-251006	00 47 18.33	-25 10 05.7	38.9 \pm 7.7	10.8 \pm 4.9	28.1 \pm 6.6	0.59 \pm 0.12	...
16	J004719.8-250643	00 47 19.76	-25 06 43.2	118.4 \pm 14.9	113.4 \pm 13.9	5.0 \pm 6.6	1.79 \pm 0.23	...
17	J004721.0-251003	00 47 20.98	-25 10 03.1	25.6 \pm 6.7	13.6 \pm 5.2	12.0 \pm 4.9	0.39 \pm 0.10	...
18	J004722.5-251200	00 47 22.49	-25 12 00.3	79.8 \pm 10.2	10.4 \pm 4.7	69.5 \pm 9.5	1.21 \pm 0.15	...
19	J004722.6-251125	00 47 22.57	-25 11 25.0	13.6 \pm 5.2	9.9 \pm 4.6	3.7 \pm 3.4	0.21 \pm 0.08	...
20	J004723.1-251054	00 47 23.15	-25 10 54.0	439.5 \pm 22.1	357.4 \pm 20.0	82.0 \pm 10.1	6.66 \pm 0.33	R9, DWH8, VP22
21	J004723.2-251122	00 47 23.24	-25 11 22.4	9.5 \pm 4.7	2.6 \pm 3.4	6.9 \pm 4.0	0.14 \pm 0.07	...
22	J004723.3-250855	00 47 23.33	-25 08 55.5	18.3 \pm 6.6	17.1 \pm 6.2	1.1 \pm 3.3	0.28 \pm 0.10	...
23	J004724.6-251214	00 47 24.55	-25 12 13.8	10.6 \pm 4.9	8.0 \pm 4.3	2.5 \pm 3.2	0.16 \pm 0.07	...
24	J004724.6-250751	00 47 24.61	-25 07 50.8	16.0 \pm 7.7	11.3 \pm 6.2	4.7 \pm 5.3	0.24 \pm 0.12	...
25	J004726.5-250832	00 47 26.52	-25 08 32.3	24.0 \pm 7.3	15.2 \pm 6.2	8.8 \pm 4.7	0.36 \pm 0.11	...
26	J004727.6-251220	00 47 27.62	-25 12 20.2	102.4 \pm 11.3	73.6 \pm 9.8	28.8 \pm 6.6	1.55 \pm 0.17	...
27	J004727.9-251243	00 47 27.88	-25 12 43.1	17.7 \pm 5.7	13.1 \pm 5.0	4.5 \pm 3.6	0.27 \pm 0.09	...
28	J004730.8-251128	00 47 30.78	-25 11 27.7	20.3 \pm 5.9	7.5 \pm 4.1	12.8 \pm 4.9	0.31 \pm 0.09	...
29	J004731.3-251127	00 47 31.26	-25 11 27.3	13.0 \pm 5.1	5.0 \pm 3.8	8.0 \pm 4.1	0.20 \pm 0.08	...
30	J004731.7-251000	00 47 31.66	-25 10 00.2	152.3 \pm 13.7	125.8 \pm 12.5	26.5 \pm 6.05	2.31 \pm 0.21	VP30

^aBackground-subtracted number of counts in each source, in each of the three energy bands (broad band: 0.3 – 8.0 keV; soft band: 0.3 – 2.0 keV; hard band: 2.0 – 8.0 keV). Count rates can be estimated by dividing the total counts by the exposure of 39558.3 s (this does not account for the vignetting, so true count rates for sources at large off-axis angles will in fact be marginally higher). Error are quoted at 68% confidence.

^bEstimated source flux, in units of 10^{-14} erg s $^{-1}$ cm $^{-2}$ and covering the 0.3 – 8.0 keV energy band, assuming the power law spectral fit to brighter X-ray sources (discussed in § 5) applies to all the sources. Assuming the same spectral model, 1 count in the soft band corresponds to a flux of 7.0×10^{-17} erg s $^{-1}$ cm $^{-2}$ (0.3 – 2.0 keV energy band), and 1 count in the hard band to 3.9×10^{-16} erg s $^{-1}$ cm $^{-2}$ (2.0 – 8.0 keV energy band). The quoted error is based on the uncertainty in source count rate, as this uncertainty dominates over the uncertainty associated with the flux estimated from the spectral model.

^cPrevious detections of these sources, based on *ROSAT* PSPC and HRI observations. The letters refer to the paper (R: Read et al. (1997), DWH: Dahlem et al. (1998), VP: Vogler & Pietsch (1999)) and the following number is the source number given in that particular paper.

TABLE 8
OPTICAL COUNTERPARTS TO X-RAY SOURCES IN THE NORTHERN HALO

ID	R^a (mag)	$\log(f_X/f_R)^b$	Notes
7	21.1	0.16	...
9	14.5	-4.05	Star
11	22.6	-0.90	...
16	14.2	-3.14	Star
18	22.8	0.10	...
19	22.8	-0.63	...
20	19.4	-0.52	AGN ^c ; $z = 1.25$
22	19.6	-1.78	...
26	21.8	-0.16	...
28	22.5	-0.60	...
29	21.4	-1.22	...
30	22.4	0.26	...

^aR-band magnitude of the optical candidate for each X-ray source (see § 2.2.1 for details).

^bThe logarithm of the 0.3 – 8.0 keV X-ray flux to optical flux ratio for each X-ray source with an optical counterpart.

^cRedshift from Vogler & Pietsch (1999).

TABLE 9
DIFFUSE X-RAY SURFACE BRIGHTNESS SIGNAL-TO-NOISE RATIOS

Aperture diameter ($''$)	$10^6 \times \Sigma_D^a$ Signal-to-noise ratio				
	2	2.5	3	4	5
Soft 0.3–2.0 keV band					
2.5	21.62	33.22	47.38	83.49	129.84
5.0	6.06	9.00	12.57	21.67	33.27
10.0	1.98	2.78	3.73	6.05	8.99
20.0	0.77	1.03	1.31	1.98	2.78
Hard 2.0–8.0 keV band					
10.0	2.65	3.72	4.99	8.11	12.07
20.0	1.01	1.35	1.73	2.65	3.73

^aX-ray surface brightness in units of counts s^{-1} arcsec^{-2} , assuming an exposure time of 39588.3 s in the soft band and 29439.6 s in the hard X-ray band.

In deriving this, we have made use of the fact that for normally distributed errors $\sigma_{H-S}^2 = \sigma_H^2 + \sigma_S^2 = \sigma_{H+S}^2$. In practice Poisson statistics should be used when dealing with X-ray hardness ratios, and this method of combining errors is not exact. As a robust hardness ratio requires ≥ 20 counts per band, the difference between Gaussian and Poisson statistics is minimal, and we employ the normal method of combination of errors for convenience.

In practice the counts in both the hard and soft bands must be modified to subtract the appropriate background counts in each energy band before making the hardness ratio. The uncertainties in the hard and soft band counts used in Equ. C1 should take the background subtraction into account.

C.2. Hardness ratio deviation significance

Hardness maps of diffuse X-ray emission from superwinds are typically created using smoothed images constructed in the hard and soft energy bands. Although visually pleasing, it is difficult to assess the statistical significance of any apparent variation in hardness seen in such images, in particular at arcminute or sub-arcminute angular scales.

Fig. 5b displays a hardness ratio deviation significance map, which measures the statistical significance of any local deviation in hardness ratio from the mean hardness ratio. We define the hardness ratio deviation significance $\Delta Q/\sigma_Q$ at any pixel i, j to be $(Q_{i,j} - Q_{\text{mean}})/\sigma_{Q_{i,j}}$, where $Q_{i,j}$ is the hardness ratio at that pixel, $\sigma_{Q_{i,j}}$ is the uncertainty in the hardness ratio at that point (as given by Equ. C1), and Q_{mean} is the mean hardness of the diffuse emission.

High significance deviations ($\Delta Q/\sigma_Q \geq 4$) are likely to indicate real spectral variation. If however, the hardness deviations are due to noise, then the number of pixels in the hardness deviation significance map as a function of $\Delta Q/\sigma_Q$ should follow a Gaussian distribution centered on $\Delta Q/\sigma_Q = 0$ with a FWHM = $2.35\Delta Q/\sigma_Q$. This method provides a convenient method of quantitatively assessing the significance of spatial variations in spectral hardness.

C.3. Diffuse emission hardness ratio deviation significances

The hardness ratio and hardness ratio deviation significance maps shown in Figs. 5 & 6 apply the method described above to the diffuse X-ray emission seen by *Chandra*.

The two energy bands for the hardness map are chosen based on the observed diffuse emission spectrum in the region of interest. For soft thermal spectra observed with the ACIS-S3 chip, the 0.3 – 0.6 keV and 0.6 – 1.0 keV energy bands are perhaps the best choice for investigating spectral variation.

For each chosen energy band we extract an image of an entire chip, with all point sources masked out. A background image in the same energy band, using the same point source mask, is also extracted from the background events file. We do *not* interpolate over the holes in the diffuse emission left by this source subtraction method, but the area affected is very small given *Chandra's* ~ 1 arcsecond spatial resolution compared to the 8.3 arcminute square chips. In order to achieve a meaningful S/N in each pixel after background subtraction, it is necessary to rebin the raw ACIS pixels by a factor of 60 or 120 in both RA. and Dec. The resulting pixels in the hardness maps are then 29.52 or 59.04 arcseconds on a side.

Each diffuse image is then background subtracted, scaling the background images by the ratio of the diffuse emission and background total exposure times. An error image, taking into account both the Poisson noise in the diffuse image and the background, is also created at this stage. The background-subtracted hard and soft band images are then combined to create a hardness map. The error images for the hard and soft bands are combined with the hardness map to create an error image for the hardness map.

A mean hardness Q_{mean} is used along with the hardness and hardness error maps to create the hardness ratio deviation significance map. For the purposes of investigating whether there is real spatial variation in the spectral properties of the diffuse emission Q_{mean} should be the mean hardness ratio over the entire region of interest.

REFERENCES

- Alton, P.B., Davies, J.J., Bianchi, S., 1999, *A&A*, 343, 51
- Anders, E., Grevesse, N., 1989, *Geochimica et Cosmochimica Acta* 53, 197
- Beck, R., Carilli, C.L., Holdaway, M.A., Klein, U., 1994, *A&A*, 292, 409
- Binette, L., Dopita, M., Tuohy, I., 1985, *ApJ*, 297, 476
- Bland-Hawthorn, J., 1995, *PASA*, 12, 190
- Bland-Hawthorn, J., Freeman, K.C. & Quinn, P.J., 1997, *ApJ*, 490, 143
- Borkowski, K.J., Lyerly, W.J. & Reynolds, S.P., 2001, *ApJ*, 548, 820
- Breitschwerdt, D., Schmutzler, T., 1999, *A&A*, 347, 650
- Carilli, C.L., Holdaway, M.A., Ho, P.T.P., De Pree, C.G., 1992, *ApJ*, 399, L59
- Castor, J., McCray, R., Weaver, R., 1975, *ApJ*, 200, L107
- Cecil, G., Bland-Hawthorn, J., Veilleux, S., Filippenko, A.V., 2001, *ApJ*, 555, 338
- Chevalier, R.A., Clegg, A.W., 1985, *Nature*, 317, 44
- Dahlem, M., Heckman, T.M., Fabbiano, G., Lehnert, M.D., Gilmore, D., 1996, *ApJ*, 461, 724
- Dahlem, M., Weaver, K.A. & Heckman, T.M. 1998, *ApJS*, 118, 401 (DWH98)
- Dahlem, M., Parmar, A., Oosterbroek, T., Orr, A., Weaver, K. A., Heckman, T. M., 2000, *ApJ*, 538, 555
- Devine, D., Bally, J., 1999, *ApJ*, 510, 197
- Dobrzyzcki, A., Ebeling, H., Glotfely, K., Freeman, P., Damiani, F., Elvis, M., Calderwood, T., 1999, in *Chandra detect 1.0 User Guide*, Cambridge: Smithsonian Astronomical Observatory
- Ekers, R.D., Sancisi, R., 1977, *A&A*, 54, 973
- Engelbracht, C.W., Rieke, M. J., Rieke, G.H., Kelly, D.M., Achtermann, J.M., 1998, *ApJ*, 505, 639
- Ferrara, A., Pettini, M., Shchekinov, Y., 2000, *MNRAS*, 319, 539
- Gehrels, N., 1986, *ApJ*, 303, 336
- Giacconi, R., et al. , 2001, *ApJ*, 551, 624
- Golla, G., Hummel, E., 1994, *A&A*, 284, 777
- Grevesse, N. & Noels, A., 1993, In *Origin of the Elements*, ed. N Prantzos, E Vangioni-Flam, M Cassé, 15, Cambridge: Cambridge Univ. Press
- Hartquist, T.W., Dyson, J.E., Williams, R.J.R., 1997, *ApJ*, 482, 182
- Heckman, T.M., 2001, to appear in “Extragalactic Gas at Low Redshift”, ed. J. Mulchaey and J. Stocke, ASP Conf. Series (astro-ph/0107438)
- Heckman, T. M., Armus, L., & Miley, G. K. 1990, *ApJS*, 74, 833
- Heckman, T.M., Dahlem, M., Eales, S.A., Fabbiano, G., Weaver, K., 1996, *ApJ*, 457, 616
- Heckman, T. M., Lehnert, M. D., & Armus, L. 1993, in *Astrophysics and Space Science Library* 188, The Environment and Evolution of Galaxies, ed. J. M. Shull & H. A. Thronson (Dordrecht: Kluwer), 455
- Heckman, T. M., Lehnert, M. D., Strickland, D. K., & Armus, L. 2000, *ApJS*, 129, 493
- Heckman, T.M., Sembach, K.R., Meurer, G., Leitherer, C., Calzetti, D., Martin, C.L., 2001, *ApJ*, 558, 58
- Hester, J.J., Raymond, J.C., Blair, W.P., 1994, *ApJ*, 420, 721
- Hoopes, C.G., Walterbos, R.A.M., Greenawalt, B.E., 1996, *AJ*, 112, 1429
- Hoopes, C.G., Walterbos, R.A.M., Rand, R.J., 1999, *ApJ*, 522, 669
- Hughes, J.P., Rakowski, C.E., Burrows, D.N., Slane, P.O., 2000, *ApJ*, 528, L109
- Kastner, J.H., Vrtilik, S.D., Soker, N., 2001, *ApJ*, 550, L189

- Keel, W.C., 1984, ApJ, 282, 75
- Koribalski, B., Whiteoak, J.B., Houghton, S., 1995, PASA, 12, 20
- Krautter, J., et al., 1999, A&A, 350, 743
- Lehnert, M.D., Heckman, T.M., 1996, ApJ, 462, 651
- Lehnert, M.D., Heckman, T.M., Weaver, K.A., 1999, ApJ, 523, 575
- Leitherer, C., Ferguson, H., Heckman, T.M., Lowenthal, J., 1995, ApJ, 454, L19
- Leitherer C., Heckman T. M., 1995, ApJS, 96, 9
- Lloyd-Davies, E. J., Ponman, T. J., Cannon, D. B., 2000, MNRAS, 315, 689
- Mac Low M.-M., McCray R., 1988, ApJ, 324, 776
- McCarthy, P.J., Heckman, T.M., van Bruegel, W., 1987, AJ, 93, 264
- Maddox, S.J., Efstathiou, G., Sutherland, W.J., Loveday, J., 1990, MNRAS, 243, 692
- Mattila, S., & Meikle, W. P. S. 2001, MNRAS, 324, 325
- Mewe R., Kaastra J. S., Liedahl D. A., 1995, Legacy, 6, 16
- Morrison, R. & McCammon, D., 1983, ApJ, 270, 119
- Nath, B.B., Trentham, N., 1997, MNRAS, 291, 505
- Norman, C., Bowen, D.V., Heckman, T.M., Blades, C., Danly, L., 1996, ApJ, 472, 73
- Persic, M., et al., 1998, A&A, 339, L33
- Pettini, M., Shapley, A. E., Steidel, C. C., Cuby, J.-G., Dickinson, M., Moorwood, A. F. M., Adelberger, K. L., Giavalisco, M., 2001, ApJ, 554, 981
- Phillips, A.C., 1993, AJ, 105, 486
- Pietsch, W., et al, 2001, A&A, 365, L174
- Pietsch, W., Trinchieri, G., Vogler, A., 1998, A&A, 340, 351
- Pietsch, W., Vogler, A., Klein, U., Zinnecker, H., 2000, A&A, 360, 24
- Ptak, A., Serlemitsos, P., Yaqoob, T., Mushotzky, R., Tsuru, T., 1997, AJ, 113, 1286
- Puche, D., Carignan, C., 1988, AJ, 95, 1025
- Puche, D., Carignan, C., van Gorkom, J.H., 1991, AJ, 101, 456
- Radovich, M., Kahanpää, J., Lemke, D., 2001, A&A, in press (astro-ph/0108075)
- Rand, R.J., 1996, ApJ, 462, 712
- Rand, R.J., 1998, ApJ, 501, 137
- Raymond, J.C., Smith, B.W., 1977, apjs, 35, 419
- Read, A.M., 1994, Ph.D. Thesis, University of Birmingham
- Read, A.M., Ponman, T.J., Strickland, D.K., 1997, MNRAS, 286, 626
- Reuter, H.-P., Klein, U., Lesch, H., Wielebinski, R., Kronberg, P. P., 1994, A&A, 282, 724
- Richter, P., Sembach, K.R., Wakker, B.P., Savage, B.D., Tripp, T.M., Murphy, E.M., Kalberla, P.M.W., Jenkins, E.B., 2001, ApJ, in press (astro-ph/0105466)
- Rosen, A., Bregman, J.N., 1995, ApJ, 440, 634
- Savage, B.D. & Sembach, K.R., 1996, ARA&A, 34, 279
- Seaquist, E.R., Odegard, N., 1991, ApJ, 369, 320
- Shoppell, P.L., Bland-Hawthorn, J., 1998, ApJ, 493, 129
- Smith, R.K., Brickhouse, N.S., Liedahl, D.A. Raymond, J.C., 2001, ApJ, 556, L91,
- Schulz, H., Wegner, G., 1992, A&A, 266, 167
- Sofue, Y., Vogler, A., 2001, A&A, 370, 53
- Sutherland, R.S., Dopita, M.A., 1993, ApJS, 88, 253
- Strickland, D.K., Heckman, T.M., Weaver, K.A., Dahlem, M., 2000, AJ, 120, 2965

- Strickland, D.K., Ponman, T.J., Stevens, I.R.,
1997, MNRAS, 320, 378
- Strickland, D.K. & Stevens, I.R., 1998, MNRAS,
297, 747
- Strickland, D.K. & Stevens, I.R. 2000, MNRAS,
314, 511
- Suchkov, A.A., Balsara, D.S., Heckman, T.M.,
Leitherner, C., 1994, ApJ, 430, 511
- Suchkov A. A., Berman V. G., Heckman T. M.,
Balsara D. S., 1996, ApJ, 463, 528
- Tomisaka, K., Bregman, J.N., 1993, PASJ, 45, 513
- Tomisaka, K., Ikeuchi, S., 1988, ApJ, 220, 695
- Tsuru, T.G., Awaki, H., Koyama, K., Ptak, A.,
1997, PASJ, 49, 619
- Tüllmann, R., Dettmar, R.-J., Soida, M., Ur-
banik, M. & Rossa, J., 2000, A&A, 364, L36
- Ulvestad, J.S. & Antonucci, R.R.J., 1997, ApJ,
488, 621
- Vogler, A., Pietsch, W., 1999, A&A, 342, 101
- Wang, J., Heckman, T.M., Lehnert, M.D., 1997,
ApJ, 491, 114
- Wang, Q.D., Immler, S., Walterbos, R., Lau-
roesch, J.T., Breitschwerdt, D., 2001, ApJ, 555,
L99
- Watson M. G., Stanger V., Griffiths R. E., 1984,
ApJ, 286, 144
- Weaver R., McCray R., Castor J., Shapiro P.,
Moore R., 1977, ApJ, 218, 377
- Weaver, K. A., Heckman, T. M., Dahlem, M.,
2000, ApJ, 534, 684
- Xia, X.-Y., Xue, S.J., Mao, S., Boller, Th., Deng,
Z.G., Wu, H., 2001, ApJ, in press (astro-
ph/0107559)
- Yun, M.S., Ho, P.T.P., Lo, K.Y., 1993, ApJ, 411,
L17